



Sridharan, B., Gurivindapalli, D., Nath Kuiry, S., Kisan Mali, V., Nithila Devi, N., Bates, P. D., & Sen, D. (2020). Explicit Expression of Weighting Factor for Improved Estimation of Numerical Flux in Local-inertial Models. *Water Resources Research*, 56(7), [e2020WR027357]. <https://doi.org/10.1029/2020WR027357>

Peer reviewed version

Link to published version (if available):
[10.1029/2020WR027357](https://doi.org/10.1029/2020WR027357)

[Link to publication record in Explore Bristol Research](#)
PDF-document

This is the author accepted manuscript (AAM). The final published version (version of record) is available online via American Geophysical Union at <https://agupubs.onlinelibrary.wiley.com/doi/full/10.1029/2020WR027357>. Please refer to any applicable terms of use of the publisher.

University of Bristol - Explore Bristol Research

General rights

This document is made available in accordance with publisher policies. Please cite only the published version using the reference above. Full terms of use are available:
<http://www.bristol.ac.uk/red/research-policy/pure/user-guides/ebr-terms/>

Explicit Expression of Weighting Factor for Improved Estimation of Numerical Flux in Local-inertial Models

B. Sridharan¹, Dinakar Gurivindapalli², Soumendra Nath Kuiry^{3,*}, Vijay Kisan Mali⁴, N. Nithila Devi⁵, Paul D. Bates⁶, and Dhrubajyoti Sen⁷

^{1,4,5}Research Scholars, Hydraulics and Water Resources Engineering Division, Department of Civil Engineering, IIT Madras, India

²Master student, Hydraulics and Water Resources Engineering Division, Department of Civil Engineering, IIT Madras, India

³Assistant Professor, Hydraulics and Water Resources Engineering Division, Department of Civil Engineering, IIT Madras, India

⁶Professor, School of Geographical Sciences, University of Bristol, University Road, Bristol BS8 1SS, UK

⁷Professor, Department of Civil Engineering, IIT Kharagpur, India

*Corresponding author: Soumendra Nath Kuiry (snkuiry@iitm.ac.in)

Key Points:

- The inertial formulation of the St. Venant equations is unstable when applied to low friction areas typical of urban environments.
- Numerical stability is improved using the diffusive term but calibration is required to obtain an optimal value of the diffusion coefficient.
- This study proposes an explicit expression for the diffusion coefficient, obviating the need for trial and error calibration.

Abstract

Two-dimensional shallow water models have been widely used in forecasting, risk assessment and management of floods. Application of these models to large-scale floods with high-resolution terrain data significantly increases the computation cost. In order to reduce computation time, shallow water models are simplified by neglecting the inertial and/or convective acceleration terms in the momentum equations. The local-inertial models have proved to significantly improve the computational efficiency even for large scale flood forecasting. However, instability issues are encountered on smooth surfaces of urban areas having low friction values. This problem was resolved by de Almeida et al. (Water Resources Research 48: 1 - 14, 2012) by introducing limited artificial diffusion in the form of weighting factors for the neighboring fluxes. The arbitrary value of the weighting factor poses a practical limitation of being case specific and requiring calibration for accurate solutions. This study derives an explicit expression for the weighting factor, an adaptive formulation dependent on local velocity, flow depth, grid and time step size, that eliminates the need for trials and approximations. Comparisons between analytical, experimental and real-world applications confirm the accuracy and robustness of the proposed weighting factor. Implementation of adaptive weights results in less computation time compared to LISFLOOD-FP (~1.2 times) and hold a significant advantage over HEC-RAS (~25.9 times) as it allows the use of larger time step at higher CFL values. The contribution of the present study therefore resolves an important problem of current large scale flood simulations, especially those implemented in real-time.

Keywords: Flood modeling; Local-inertial model; Adaptive weighting factor; Chennai flood 2015

1 Introduction

Flood inundation is considered as a major natural hazard. Its accurate prediction is therefore necessary for developing flood hazard zone maps and issuing warnings before the occurrence of extreme flood events. Mathematical models simulating the physics thus play a pivotal role in these flood risk assessment tools. Most models solve the depth-averaged two-dimensional (2D) shallow water equations (SWEs) and in the past few decades, substantial research has gone into the development of various numerical schemes that form the basis of these models (Peraire et al., 1986; Bermudez et al., 1991; Hubbard, 1999; Sanders et al., 2008; Liang, 2010; Cea and Blade, 2015). In spite of the high-computational power and substantial progress in numerical methods, application of these models to large-domain with high-resolution topographical details, especially for issuing early warnings, demands high computation time (de Almeida et al., 2012). Simulation at high-resolution is particularly important in urban areas for capturing the complex hydrodynamic processes with a detailed representation of topographical features (Horritt and Bates, 2001; Brown et al., 2007; Fewtrell et al., 2008; Neal et al., 2009; Horritt et al., 2010; Sampson et al., 2012). This indicates the limitations of using complete 2D models for simulating floods over large areas at high resolution. In order to reduce the computational burden, four different speed-up approaches are currently employed: (i) high-performance parallelization approach that takes advantage of general purpose graphics processing unit (GPGPU) (Kalyanapu et al., 2011), distributed memory parallelization (Pau and Sanders, 2006, Neal et al., 2009), multi-core central processing units (MCs), cloud computing (Lamb et al., 2009), etc.; (ii) a simplified hydraulic model approach, in which one (i.e. convective acceleration) or both inertial terms from the complete 2D SWEs are ignored to obtain either a diffusion wave (Bates and De Roo, 2000) or a local-inertial model (de Almeida et al., 2012); (iii) a coarse-grid approach, in which the computation time is reduced either by increasing the grid size or using techniques like sub-grid treatment (Yu and Lane, 2011) and

porosity parameter (Sanders et al., 2008; Bruwier et al., 2017) to compensate for loss of accuracy; and (iv) the Cellular Automata (CA) approach (Dottori and Todini, 2010; Guidolin et al., 2016), in which the computational efficiency is improved using the universal transition rule for spatial discretization. This study attempts to use the simplified hydraulic model approach, which can render a much reduced computation time if implemented using techniques like GPGPU, parallelization or sub-grid approach. The diffusive or local-inertial models adopt simpler numerical methods for its solution algorithm. As a result, the computational cost of simplified models for each time step is significantly reduced in comparison to the equivalent numerical solution of full 2D models (Bates et al., 2010; de Almeida et al., 2012; Shustikova et al., 2019). This improvement in computational efficiency has allowed the use of simplified models to a new range of applications, such as Monte Carlo simulations for estimating uncertainty (Aronica et al., 2002) and ensemble simulations for flood forecasting (Pappenberger et al., 2005).

Of the two simplified SWE formulations that have been developed, the local-inertial formulation provides a better alternative to the diffusive wave approximation. The main advantage of the local-inertial formulation lies in the improved stability condition that can be used to determine the time step. The time step for the local-inertial model reduces linearly with grid size, unlike diffusive wave models where the time step decreases quadratically (Bates et al., 2010). This is because the local-inertial formulation is a shallow water model and the time step is therefore controlled by the Courant-Friedrichs-Lewy (CFL) condition, rather than the more restrictive time step constraint necessary for the diffusion wave equation developed by Hunter et al. (2005). This property of local-inertial models thus substantially enhances the computational efficiency even for problems with fine grids that would have been prohibitively expensive to be solved with diffusive models. Also, it avoids the dramatic reduction in time step that is usually the case for diffusive wave models in regions of negligible water surface gradient. Several local-inertial models have been developed based on different numerical schemes (Ponce, 1990; Xia, 1994; Aronica et al., 1998; Bates et al., 2010; Martins et al., 2015). Among these, the scheme proposed by Bates et al. (2010) for solving the local-inertial equations is widely used for its relative simplicity and low computation cost. Recent versions of the local-inertial model, LISFLOOD-FP, are based on the numerical solution scheme given by Bates et al. (2010). This scheme has been successfully used for flood inundation modeling in various parts of the world such as Europe (Bates et al., 2010), West Africa (Neal et al., 2012), the Amazon (Baugh et al., 2013), India (Sanyal et al., 2013; Lewis et al., 2013) and North Africa (Yan et al., 2014). The European Flood Awareness System (<https://www.efas.eu/>) uses LISFLOOD-FP as its hydraulic model for the flood forecasting of entire Europe. The landscape evaluation model CAESAR-LISFLOOD (Coulthard et al., 2013) uses the local-inertial formulation of Bates et al. (2010) for its hydraulic simulation. MGB-IPH is another model that uses the same solution scheme of Bates et al. (2010) for flow routing and has been applied for large-scale flood simulations (de Paiva et al., 2013; Pontes et al., 2017). CaMa-Flood, which is a global river model, developed by Yamazaki et al. (2013) also uses the local-inertial formulation. These local-inertial models run on the scheme proposed by Bates et al. (2010) and are shown to outperform both diffusive as well as full 2D models in terms of computational efficiency for sub-critical flows (Neal et al., 2012; de Almeida et al., 2013).

Despite its high performance, the solution scheme was reported to suffer from numerical instability under certain flow conditions in low friction regions such as urban areas (Bates et al., 2010). In order to overcome this issue, de Almeida et al. (2012) proposed an improvement by introducing an artificial diffusive term for accurate estimation of the numerical flux. The numerical diffusion

is added to the flux computed through an interface of a computational cell using the discharge values of the neighboring interfaces. The amount of diffusion is limited and controlled by a weighting factor (θ) which is effectively a diffusion coefficient (de Almeida et al., 2012). Two numerical schemes (q-schemes), namely, upwind and centered schemes were proposed by de Almeida et al. (2012) based on the way the weight is applied to the flux calculations. These schemes were shown to provide smooth solutions even for a wide range of friction values (down to values of Manning's friction coefficient (n) of $0.01 \text{ m}^{-1/3}\text{s}$), unlike the numerical solution of Bates et al. (2010) which had a tendency to break down for values of $n < 0.03 \text{ m}^{-1/3}\text{s}$. However, the accuracy of the solution depends on the value of the parameter θ , which is chosen empirically. It is observed from the applications of the LISFLOOD-FP model that stable solutions are obtained for the range $0.7 < \theta < 1.0$. Since the value of θ controls the amount of diffusion, that is the flux, its value needs to be optimized through trial and error. Martins et al. (2015) have argued that this poses a problem since the calibration procedure makes use of real-world data for obtaining the best value of θ . To overcome this issue, they proposed a well-balanced local-inertial model, in which the mass and momentum fluxes are computed using the Riemann solver. Although this model avoids the requirement of the trial and error procedure, it is computationally ~ 4.0 times more expensive compared to the scheme proposed in de Almeida et al. (2012) and subsequently implemented in LISFLOOD-FP. This motivates formulating an explicit expression for θ to be used in local-inertial models such as LISFLOOD-FP. Such an expression is derived in this paper based on the local flow dynamics at each computational cell boundary and eliminates the need for the trial and error approximation of θ . Considering the range of applications an explicit expression for estimating the value of θ is expected to improve the accuracy and numerical stability of LISFLOOD-FP model.

This study, therefore, aims at formulating an expression for θ to automatically control the amount of diffusion for calculating flux in the solution scheme of de Almeida et al. (2012). The value of θ varies both spatially and temporally, adapting itself automatically with those of the local variables. The adaptive expression for θ is then implemented into the upwind and centered schemes, also termed as s-schemes, of the local-inertial formulations as described in de Almeida et al. (2012). The accuracy is first verified by solving a 1D analytical test case. The 2D flood flows observed in an experimental river-network-floodplain setup is simulated to demonstrate the effect of θ on the performance of s-schemes and the LISFLOOD-FP model. Then a real-time urban flood event in Glasgow, UK, is simulated to show the improved stability condition of adaptive θ based s-schemes compared to the use of constant θ in q-scheme of de Almeida et al. (2012). Finally, s-schemes are applied to one of the most devastating floods in the history of Chennai city in Southern India that occurred in 2015. It is observed that the proposed adaptive θ for local-inertial model not only automatically controls the amount of diffusion but also increases the computational time step size as and when required. As a result, a significant reduction in computation time is also achieved in the reported applications compared to LISFLOOD-FP. The detailed analyses and comparisons of results imply that the contribution of this study in formulating an explicit expression for adaptive θ improves accuracy, computational efficiency and stability of a local-inertial model.

2 Governing Equations

The governing equations for the proposed model are derived by simplifying the 2D SWEs. The simplification is primarily based on the assumption that for slowly varying flows the convective acceleration terms can be neglected (de Almeida et al., 2012) and the resulting system of local-inertial equations can be written as

$$\frac{\partial h}{\partial t} + \frac{\partial q_x}{\partial x} + \frac{\partial q_y}{\partial y} = 0 \quad (1)$$

$$\frac{\partial q_x}{\partial t} + gh \frac{\partial H}{\partial x} + \frac{gn^2 |q_x| q_x}{h^{7/3}} = 0 \quad (2)$$

$$\frac{\partial q_y}{\partial t} + gh \frac{\partial H}{\partial y} + \frac{gn^2 |q_y| q_y}{h^{7/3}} = 0 \quad (3)$$

where t is the time; x and y are the Cartesian directions; h is the water depth, q_x and q_y are the unit width discharges in the x - and y -directions, respectively; $H = h + z$ is the water surface elevation; z is the bed elevation with respect to a datum and g is the acceleration due to gravity. The numerical scheme adopted herein uses the simplified momentum equations (2) and (3) in the two spatial directions for updating corresponding unit discharges, which in turn are used to compute mass fluxes in equation (1). In the next step, equation (1) is used to update the unknown water surface elevation at the cell centroid. The numerical discretization of the above governing equations is discussed in the following section.

3 Numerical scheme

The computational domain is described by a structured grid (Figure 1) which has the advantage to exploit the expanding wealth of raster terrain data. The mass and simplified inertial momentum equations are discretized using the Godunov like approach, in which the mass fluxes are computed through the interfaces ($i \pm 1/2$ and $j \pm 1/2$) of a cell using a simple analytical equation and the water depth is updated at the cell center (i, j) (de Almeida et al., 2012).

Equation (1) is discretized for a computational cell as shown in Figure 1 using a first-order forward time marching scheme as follows

$$\frac{h_{i,j}^{t+\Delta t} - h_{i,j}^t}{\Delta t} = \frac{q_{i-1/2,j}^{t+\Delta t} - q_{i+1/2,j}^{t+\Delta t}}{\Delta x} + \frac{q_{i,j-1/2}^{t+\Delta t} - q_{i,j+1/2}^{t+\Delta t}}{\Delta y} \quad (4)$$

where Δx and Δy are the cell sizes in the x - and y -directions, respectively; Δt is the time step size; $h_{i,j}^t$ and $h_{i,j}^{t+\Delta t}$ are the water depths at the cell centroid in the current and next time steps respectively; $q_{i+1/2,j}^{t+\Delta t}$ and $q_{i-1/2,j}^{t+\Delta t}$ are the mass fluxes through the interfaces ($i \pm 1/2, j$) along the x -direction; and $q_{i,j+1/2}^{t+\Delta t}$ and $q_{i,j-1/2}^{t+\Delta t}$ are the mass fluxes through the interfaces ($i, j \pm 1/2$) along the y -direction. The mass flux $q^{t+\Delta t}$ at an interface is computed after solving the corresponding momentum equation.

The local-inertial momentum equations (2) and (3) are also similarly discretized, for example, the flux along the x -direction at the interface $(i-1/2, j)$ is written using equation (2) as

$$\frac{q_{i-1/2,j}^{t+\Delta t} - q_{i-1/2,j}^t}{\Delta t} + gh_{flow}S_t + \frac{gn^2|q_{i-1/2,j}^t|q_{i-1/2,j}^t}{h_{flow}^{7/3}} = 0 \quad (5)$$

where, $S_t = \partial H / \partial x$ is the water surface gradient and h_{flow} represents the effective flow depth across the interface $(i-1/2, j)$. The effective flow depth at an interface is estimated as $h_{flow} = \max(H_{i,j} - H_{i-1,j}) - \max(z_{i,j} - z_{i-1,j})$. Hence, equation (5) may now be used to explicitly compute $q_{i-1/2,j}^{t+\Delta t}$ at an interface using the known values of q^t , h^t and z . A further improvement may also be made in equation (5) by replacing one q^t in the friction term by $q^{t+\Delta t}$, as instabilities may still arise at shallow depths (e.g. near the wet-dry interface), where the friction term becomes too large (Bates et al., 2010; Kuiry et al., 2010). This substitution leads to an explicit equation for the unknown $q_{i-1/2,j}^{t+\Delta t}$ with improved convergence properties similar to that of an implicit time stepping scheme. Rearranging terms, equation (5) reads as under:

$$q_{i-1/2,j}^{t+\Delta t} = \frac{q_{i-1/2,j}^t - gh_{flow}\Delta t S_t}{\left(1 + gn^2\Delta t|q_{i-1/2,j}^t|/h_{flow}^{7/3}\right)} \quad (6)$$

Equation (6) is used to compute mass fluxes through the interface, $(i-1/2, j)$. Similarly, fluxes through the other three interfaces of the cell (i, j) can be obtained by following the above discretization procedure. Once the fluxes are computed, equation (4) is used to explicitly update the unknown flow depth at the center of a cell, $h_{i,j}^{t+\Delta t}$. The solution methodology followed here is similar to the semi-implicit scheme proposed by Bates et al. (2010). Equation (6) improves the computational efficiency significantly due to the fact that the time step is computed using the CFL condition instead of the more restrictive time step constraint proposed by Hunter et al. (2005). However, the finite difference technique of discretizing the spatial derivatives leads to lack of diffusive terms. As a result, the scheme suffers from numerical instability at low friction values ($n < \sim 0.03$) as the dampening effect reduces. de Almeida et al. (2012) conducted a detailed study for counteracting the instabilities by incorporating a diffusion like term in equation (6). The diffusion term is in fact a modification of $q_{i-1/2,j}^t$ in the numerator of equation (6) by taking the contribution of fluxes from the neighboring cells. In effect, such a modification improves the estimation of fluxes through a cell boundary by considering a larger stencil in a similar way to that of upwind and centered schemes. However, this simple modification in equation (6) has been shown to yield a large improvement in the numerical stability of the local-inertial models (de Almeida et al., 2012) at low friction values.

3.1 Numerical schemes with diffusive terms

de Almeida et al. (2012) proposed two schemes (i.e. q -schemes), termed as (a) q -upwind and (b) q -centered, depending on the way the information from the neighboring cell(s) is used to introduce the dissipation effect. For example, in case of the q -upwind scheme, flux at the interface $(i-1/2, j)$ - $q_{i-1/2,j}^{t+\Delta t}$, is obtained by adding a small amount of flux from either the left or right of

its neighboring interfaces based on the direction of flow. The modified flux equation at an interface is thus computed as

$$q_{i-1/2,j}^{t+\Delta t} = \begin{cases} \frac{\theta q_{i-1/2,j}^t + (1-\theta)q_{i-3/2,j}^t - gh_{flow}\Delta t S_t}{\left(1 + gn^2\Delta t |q_{i-1/2,j}^t| / h_{flow}^{7/3}\right)} & \text{if } q_{i-1/2,j}^t > 0 \\ \frac{\theta q_{i-1/2,j}^t + (1-\theta)q_{i+1/2,j}^t - gh_{flow}\Delta t S_t}{\left(1 + gn^2\Delta t |q_{i-1/2,j}^t| / h_{flow}^{7/3}\right)} & \text{if } q_{i-1/2,j}^t < 0 \end{cases} \quad (7)$$

For the q-centered scheme, the weighting of fluxes from both neighboring interfaces is used to stabilize the solution. The flux $q_{i-1/2,j}^{t+\Delta t}$, for example, is computed as

$$q_{i-1/2,j}^{t+\Delta t} = \frac{\theta q_{i-1/2,j}^t + (1-\theta)\left(\frac{q_{i-3/2,j}^t + q_{i+1/2,j}^t}{2}\right) - gh_{flow}\Delta t S_t}{\left(1 + gn^2\Delta t |q_{i-1/2,j}^t| / h_{flow}^{7/3}\right)} \quad (8)$$

In equations (7) and (8), θ is the empirical flux weighting factor. The terms associated with $(1-\theta)$ in the same equations are called the diffusive terms. The value of θ controls the amount of dissipation and gives non-oscillatory water surface profile when an appropriate value for θ is chosen. With $\theta=1$, the semi-implicit scheme of Bates et al. (2010) is obtained, which is found to give numerical instability for $n < 0.03 \text{ m}^{-1/3}\text{s}$ (de Almeida et al., 2012). $\theta=0$ results in a scheme similar to the Lax diffusive. de Almeida et al. (2012) used a constant value for θ (such as, 0.8 and 0.9) to improve the stability for the test cases in their study. However, this constant value needs to be fixed for each case through a trial process. The derivation of the proposed closed-form solution for θ , which being based on the local flow characteristics obviates the need for its ad hoc selection, is presented in the following section.

3.2 Expression for adaptive theta

The terms of q-schemes given by equations (7) and (8) are inspired by the concept of upwinding and centered schemes, respectively (de Almeida et al., 2012). These equations mainly use the direction of flow (i.e., towards left or right along x -direction and towards top or bottom along y -direction) to obtain the artificial diffusive terms but neglect the directions of individual waves, as in the case of the full SWEs. Hence, considering the similarities with upwind and centered schemes (de Almeida et al., 2012), the same names are used in this study. However, it is important to note that the inclusion of the diffusive terms in equations (7) and (8) is akin to the concept of the weighted average flux (WAF) method (Toro, 2001). Ying et al. (2004) used a similar concept of applying weights computed from the CFL number as a function of velocity, time step and grid size, to remove oscillations associated with the centered discretization of the bed slope terms. Following the concept of Ying et al. (2004), a simple expression as given below, is proposed here for computing the weighting factor.

$$\theta_{i-1/2,j} = 1 - c_{i-1/2,j}^r \quad (9)$$

and

$$c_{i-1/2,j}^r = \frac{\Delta t}{\Delta x} u_{i-1/2,j} \quad (10)$$

where $c_{i-1/2,j}^r$ is the interface CFL number.

The CFL number is generally used as the criteria for stability in shallow water models and the minimum value of CFL within a time step is obtained by a heuristic search through all the cells of the computational domain. However, implementation of a minimum value of CFL and subsequently a single value of θ at all cell interfaces is found to under/over predict the solution, as in de Almeida et al. (2012). One possible reason could be that the flux at all the interfaces cannot be scaled by a single value of θ as it may not consider the effect of local flow dynamics. Therefore, it is proposed to compute θ at all the interfaces at each time step considering the local flow velocity and water depth for better accuracy. Since local-inertial models do not compute velocity as a solution variable, the velocity at a typical interface, for example $u_{i-1/2,j}$ (Figure 1) is obtained from the calculated discharge value as,

$$u_{i-1/2,j} = \frac{|q_{i-1/2,j}|}{h_{flow}} \quad (11)$$

The expression of the diffusion coefficient thus becomes

$$\theta_{i-1/2,j} = 1 - \frac{\Delta t}{\Delta x} u_{i-1/2,j} \quad (12)$$

It is found that near the wet-dry interface, θ may become very small or even negative as the second term on the right side of equation (9) may turn out to be greater than unity. For that reason, the wave celerity at the interface is also considered and the expression for θ is redefined as

$$\theta_{i-1/2,j} = 1 - \frac{\Delta t}{\Delta x} \min(u_{i-1/2,j}, \sqrt{gh_{flow}}) \quad (13)$$

It can be observed from equation (13), that more diffusion from the neighboring interface is introduced when the flow velocity is high, while it tends to be zero in the region having negligible water surface slope. Since this weighting factor is likely to change both spatially and temporally depending upon the value of discharge and water depth, it may be referred to as “*adaptive weighting factor*” or simply “*adaptive θ* ”. The proposed expression for θ as given in equation (13) is substituted in equations (7) and (8) and the modified form of q-schemes (q-centered and q-upwind) are re-named as s-schemes (s-upwind and s-centered) in this study. Though the proposed s-schemes involve a few extra computations compared to q-schemes, the numerical experiments presented subsequently prove that improved numerical stability achieved at higher CFL numbers to compensate the additional computational cost. Martins et al. (2015) also neglected the convective acceleration term aiming to reduce the computation time of a full 2D model by applying a well-balanced Roe scheme for computing mass and momentum fluxes through each cell interface. Following this, the momentum and water depth at the cell centroids are updated. However, the present implementation of the same scheme proves that the use of the shock-capturing algorithm of Roe results in more than twice the computation time compared to the local-

inertial schemes. This is quite obvious since local-inertial models do not solve the mass and momentum equations separately and the Roe scheme based finite volume solution is restricted by CFL number (Kuiry et al., 2008). Therefore, the proposed adaptive θ has the potential to improve the numerical stability of local-inertial models and also to reduce the overall computation time.

4 Stability condition

The model time step is evaluated as suggested in Bates et al. (2010)

$$\Delta t = \alpha \frac{\Delta x}{\sqrt{gh_{\max}}} \quad (14)$$

where h_{\max} is the maximum depth at any time step and α is the CFL number. The s-schemes are run with $\alpha = 0.9$ for stable results and are reported herein. Both the q-schemes (de Almeida et al., 2012) have been coded in the present model since q-upwind scheme is not available in LISFLOOD-FP (version 5.8.9). The q-schemes implemented by the authors as well as the q-centered scheme in LISFLOOD-FP show numerical oscillations for $\alpha = 0.9$, hence $\alpha = 0.8$ is used for all the test cases.

5 Model testing and results

The performance of the proposed adaptive θ in inertial models is assessed through a variety of numerical tests as follows

- (i) Nonbreaking wave propagation over a horizontal plane
 - (ii) Nonbreaking wave propagation on a planar beach
 - (iii) Steady flood flow in a river-network-floodplain setup
 - (iv) An urban flood event in Glasgow, UK
 - (v) Chennai (India) flood of 2015
- } Analytical tests
 } Experimental tests
 } Applications

The results of the s-schemes are compared with those obtained from analytical solutions, LISFLOOD-FP (de Almeida et al., 2012), full dynamic version of HEC-RAS 2D (Brunner, 2016), TELEMAC 2D (Hervouet, 2000) and the results reported in Hunter et al. (2008).

5.1 Non-breaking wave propagation on a horizontal plane

This case is simulated here to assess the sensitivity of θ in q-schemes and the proposed adaptive θ in s-schemes on overall accuracy when Manning's roughness is varied from smooth surface to a numerically challenging low value. Hunter et al. (2005) developed an analytical solution for this problem by simplifying the full Saint-Venant equations, where water depth is expressed as a function of space and time as given below.

$$h(x, t) = \left[\frac{7}{3} (C - n^2 u^3 (x - ut)) \right]^{3/7} \quad (15)$$

where u is the constant velocity along the x -direction, n is the Manning's roughness coefficient, and C is an integration constant which can be obtained using $h(u, t) = 0$. The upstream boundary condition of time-varying depth is imposed at $x = 0$ as

$$h(0, t) = \left(\frac{7}{3} n^2 u^3 t \right)^{3/7} \quad (16)$$

The computation domain consists of 32×240 square cells each of size $25 \text{ m} \times 25 \text{ m}$. The upstream boundary condition is imposed along the entire width of the domain and as a result the problem reduces to 1D wave propagation along the x -direction. Two simulations are performed with different Manning's coefficients, $n = 0.01$ and $0.005 \text{ m}^{-1/3}\text{s}$, with upstream velocities, $u = 0.4$ and 0.635 m/s respectively. These velocities and roughness coefficients are chosen to maintain the same boundary condition as given by equation (16). The friction value of $0.01 \text{ m}^{-1/3}\text{s}$ is chosen to represent smooth surfaces (e.g., the cemented surface in urban areas) and the very low friction of $0.005 \text{ m}^{-1/3}\text{s}$ is chosen to investigate the ability of the proposed schemes in providing oscillation-free solutions under a numerically challenging condition. The simulations are run for a duration of 9000 s . Since q-upwind scheme is not available in the recent version of LISFLOOD-FP, the q-schemes implemented by authors and the analytical solutions are used here for comparison.

Figures 2a and 2b compare the water surface profiles of the q-schemes for $\theta = 0.8$ and 0.9 with the proposed s-schemes and the analytical solutions at different instants of time. Figures 2c and 2d show the magnified views of the wavefront in Figures 2a and 2b at time $t = 9000 \text{ s}$. The q-centered and s-centered schemes are seen to propagate the wave front with almost the same accuracy but slightly slower than the corresponding analytical solutions for both the n values. It is interesting to note from Figures 2e and 2f that during the entire simulation period, the average adaptive θ values for the s-centered scheme are 0.87 and 0.80 (Figure 2e and 2f) for $n = 0.01$ and $0.005 \text{ m}^{-1/3}\text{s}$, respectively. Also, these values are close to the fixed values of 0.90 and 0.80 for θ used by de Almeida et al. (2012) in their q-centered scheme. In addition, it should be noted that the q-centered scheme is almost insensitive to the value of θ within the considered range.

Figure 2c shows that for $\theta = 0.9$ and $n = 0.01 \text{ m}^{-1/3}\text{s}$, the wave front propagation obtained using the q-upwind scheme falls closer to the analytical solution and it is over predicted for $\theta = 0.8$. However, the simulated wave front propagation by the q-upwind scheme for $n = 0.005 \text{ m}^{-1/3}\text{s}$ with both the fixed values of θ are slower than the analytical solution as shown in Figure 2d. Hence, it is clear that for various Manning's n , the q-upwind scheme is sensitive to the θ value, de Almeida et al. (2012) reported that the q-upwind scheme is sensitive due to the zero-th order term and dropped this scheme from the LISFLOOD-FP model. Interestingly, the s-upwind scheme consistently performs better for both the n values and the wave fronts are always closer to the analytical solutions. This is due to the usage of adaptive θ following the local hydrodynamics such as velocity as shown in Figures 2e and 2f.

It is also observed that the results obtained using the q-schemes fall closer to the s-schemes, provided the adaptive θ value throughout the simulation period varies within a narrow range and the empirically fixed θ value is chosen from that specific bound of values rather than from a wide range. In this test case, though the s-upwind scheme is shown to be more accurate than the fixed

θ based q-upwind scheme, the improved accuracy of the s-centered scheme over the q-centered scheme is marginal.

For stable results, the s-schemes and q-schemes were run with time steps of 11.68 s and 9.8 s respectively. Therefore, s-schemes have been proven to be faster than q-schemes by ~1.19 times, which is about ~19% improvement in overall computation time.

5.2 Non-breaking Wave Runup on a Sloping Beach

This test case proposed by Hunter et al. (2005) explores the propagation of a wave over an adverse longitudinal slope. This test case examines the numerical stability of the proposed s-schemes as the reduction in water depth along the adverse slope enhances the non-linear effect that in turn leads to more shocks. The solution for this problem can be obtained by using a fourth order Runge-Kutta method as described in de Almeida et al. (2012). The computational domain is again discretized into 32×240 square cells each of size 25 m \times 25 m and along the longitudinal direction the adverse slope of 10^{-3} is maintained. Two simulations are performed using the Manning's coefficients, $n = 0.03$ and $0.01 \text{ m}^{-1/3}\text{s}$ and the velocity of $u = 0.4 \text{ m/s}$ is used at the upstream for both the simulations. In the absence of q-upwind scheme in the recent version of LISFLOOD-FP, the q-schemes implemented by the authors and the analytical solution are used for comparisons. Figures 3a and 3b show the comparisons of the simulated water surface profiles along the x -direction with the Runge-Kutta solution at different instants of time.

Figures 3c and 3d show the magnified views of Figures 3a and 3b, respectively at time $t = 3600 \text{ s}$. For both the n values, the s-schemes produce smooth solutions without any numerical oscillations similar to the q-schemes as reported in de Almeida et al. (2012). The water surface profiles obtained by all the centered schemes are under-predicted and the wave front propagation is slower compared to the corresponding Runge-Kutta solutions. In case of the q-upwind scheme, for $\theta = 0.8$, the water surface profile is over predicted and accordingly the wave front moves faster. The water surface profile and wave front are closer to the Runge-Kutta solution for $\theta = 0.9$ as shown in Figures 3c and 3d. On the other hand, the results of the proposed s-upwind scheme are found to be consistently closer to the Runge-Kutta solutions for both the n values, similar to the previous test case. It can be observed that again the results from the q-schemes fall closer to those of s-schemes provided the fixed value of θ (0.90 for both q-centered and q-upwind schemes) is chosen from the narrow range of the adaptive θ values (average θ of 0.91 and 0.93 for q-centered and q-upwind schemes, respectively) over the entire simulation period. The s-schemes are observed to be ~1.15 and ~1.20 times faster than the q-schemes for $n = 0.01$ and $0.03 \text{ m}^{-1/3}\text{s}$, respectively.

The above two test cases prove that the proposed adaptive θ concept gives results with either similar or better accuracy with less computation time compared to the q-schemes of de Almeida et al. (2012) irrespective of the type of schemes and Manning's roughness values. The advantage of the proposed adaptive θ concept is that the trial and error procedure required to fix θ value is completely eliminated. In addition, it is found that q-upwind scheme is also consistent provided that θ is chosen adaptively as provided in this study.

5.2 Experimental Flood Propagation in a River-Network-Floodplain Setup

The above test cases demonstrate the performance of the proposed s-schemes for 1D flow problems. It was found that in the case of 1D flow if the fixed θ value is chosen from the narrow

range of adaptive θ , the wave front computed by the q-schemes are closer to that of s-schemes. To further assess the performance of s- and q-schemes for 2D flow problems, simulations are run to reproduce the experimental flood event generated in a physical setup at the Hydraulics Laboratory of Indian Institute of Technology Madras (IITM), India (Figure. 4). The physical model represents a typical river-network-floodplain system, as commonly seen in delta regions. The setup is 20 m long and 5 m wide, and consisting of 8 channels, 4 junctions and 5 distinct floodplains (F1-F5). The channels are rectangular in section and are connected to the flood plains on either side. All the channels slope downstream with a uniform bed slope of 1:1000. The digital topography of the setup is represented by an elevation model (DEM) of 2 cm \times 2 cm resolution. More details on the DEM of the setup can be found in Mali and Kuiry (2018).

Water is released into the setup at its upstream through the main channel from an overhead tank using two pipelines of diameters 8" (203.2 mm) and 3" (76.2 mm), respectively. The discharge of water is measured using an electromagnetic flow meter. The flow rate is controlled using a sluice gate in the 8" (203.2 mm) diameter pipe and a SCADA (supervisory control and data acquisition) system in the 3" (76.2 mm) diameter pipe. The test cases are conducted for a steady-state flow of 0.078 and 0.098 m³/s. Initially, a small amount of water at a rate of about \sim 0.018 m³/s is released into the model for one hour until initial disturbances dampen out. The inflow is then gradually increased up to 0.078 and 0.098 m³/s in a sufficiently long duration. The SCADA control is used to avoid unnecessary wetting of the floodplains and subsequently to improve the accuracy of delineated flood extent using the image processing technique. Once steady state is attained water depths are measured using point gauges. The observation locations in the river (green colour) and over the floodplains (light yellow colour) are shown in Figure 4. The inundation extent is captured using a Nikon D5300 DSLR camera from the top. Finally, the captured images are processed in ARCGIS to delineate the inundation extent. Each experiment takes about 10 hours to complete and are repeated thrice to ensure the reliability of the observed water depths as well as the generated inundation extent maps. The details of the experiment can be found in Mali and Kuiry (2019).

Calibration of Manning's n value

To calibrate Manning's coefficients for LISFLOOD-FP and the proposed s-schemes the simulations are conducted using the steady-state flow of 0.078 m³/s. For calibration purpose, Manning's coefficient is varied between 0.008-0.014 m^{-1/3}s for smooth concrete surface with an increment of 0.001. In case of the LISFLOOD-FP model, apart from Manning's coefficients, different θ values are also needed to be calibrated. The value of θ is chosen between 0.70 - 0.95 with an incremental step of 0.05. Hence, the LISFLOOD-FP model was run forty-two times using the combinations of Manning's roughness coefficients (0.008-0.014 m^{-1/3}s) and weighting factors (0.70 - 0.95), while the proposed s-schemes are run only for seven values of Manning's coefficient. The simulations are carried out using the discharge of 0.078 m³/s at the upstream and measured water levels (locations shown as red dots in Figure 4) at three downstream outlets. The initial condition of the model was set by specifying a uniform water depth of 0.08 m inside the river network. The optimal value of Manning's coefficients for the LISFLOOD-FP and s-schemes are identified by comparing the simulated inundation extents with observed maps. The simulated water depth using optimal Manning's coefficients of the LISFLOOD-FP and s-schemes are then compared with observed water depths to analyze their accuracy.

The accuracies of the s-schemes and the LISFLOOD-FP model in predicting the flood extent are examined based on the number of wet/dry cells. For quantitative evaluation, the goodness-of-fit (F) values are computed using the simulated and observed inundation extents. The following expression used in Bates et al. (2006) and Kuiry et al. (2010) is adapted in this study to evaluate the measure of fit (F) value as,

$$F = \frac{A}{A + B + C} \times 100 \quad \% \quad (17)$$

where A is the wet area correctly predicted by an inertial model, B and C are the over- and under-predicted areas by a model compared to the observed data. Therefore, the value of F varies from 0 to 100 %. $F = 0$ % indicates no overlap of the predicted and observed areas and $F = 100$ % indicates a perfect overlap.

From the simulations, it was found that the LISFLOOD-FP model significantly over-predicts the inundation extent at the upstream of the flood-plain F1 when the Manning's coefficient is greater than 0.009 and the value of θ is less than 0.95. The observed inundation map indicates that this prediction is unphysical and apparently is caused by the use of high diffusion value (low weighting factor) and Manning's coefficient. As a result of this over prediction, the accuracy of simulated flood extent is reduced and F value is found to be less than 66%. On the other hand, the LISFLOOD-FP result shows significant under-prediction of inundation extent for $\theta = 0.95$, irrespective of Manning's coefficients and the F values are in the range of ~56 - 68%. The realistic inundation extents are simulated for Manning's coefficients of 0.008 and 0.009 $\text{m}^{-1/3}\text{s}$. Among these two values, a better prediction is obtained only for Manning's coefficient of 0.009 $\text{m}^{-1/3}\text{s}$ with $F = 76\%$ (for 0.008 $\text{m}^{-1/3}\text{s}$ the F value is 73%) when $\theta = 0.90$. However, when $\theta = 0.85$ these two Manning's coefficients produced overprediction of inundation extents ($F = 68\%$ for 0.008 and 66% for 0.009 $\text{m}^{-1/3}\text{s}$). Hence, 0.009 $\text{m}^{-1/3}\text{s}$ is treated as the calibrated value for the LISFLOOD-FP model. Similarly, the calibration process is carried out for s-schemes by taking value of Manning's coefficient within the range of 0.008-0.014 $\text{m}^{-1/3}\text{s}$. From the simulations, it was found that Manning's coefficient of 0.01 $\text{m}^{-1/3}\text{s}$ results in better prediction ($F = 84\%$ and 86% for s-centered and s-upwind schemes, respectively) and is thus taken as the calibrated value. These calibrated Manning's coefficients are then used to simulate the steady-state flow of 0.098 $\text{m}^{-1/3}\text{s}$ for assessing the performance of LISFLOOD-FP and s-schemes. The dependency of θ on the accuracy of the LISFLOOD-FP model and the solution to this problem given by s-schemes are discussed in the following sections.

Steady-state experimental flood caused by inflow of 0.078 m^3/s in a set-up

To demonstrate the effect of θ on accuracies, the results of LISFLOOD-FP model obtained with the calibrated n value of 0.009 $\text{m}^{-1/3}\text{s}$ for $\theta = 0.85, 0.90$ and 0.95 are discussed along with the results of s-schemes obtained using the optimal n value of 0.01 $\text{m}^{-1/3}\text{s}$. The comparison of simulated maximum inundation extent maps obtained from these two models are shown in Figure 5. The observed inundation extent is shown in red solid line (Figure 5). For $\theta = 0.85$, the LISFLOOD-FP model produces over-prediction of the inundation extent (Figure 5a) at the upstream part of the floodplain F1. The over prediction is unphysical and occurred due to the use of the constant value of θ . For $\theta = 0.9$, the LISFLOOD-FP model shows better prediction as shown in Figure 5b. A higher value of θ as 0.95 (Figure 5c) conversely leads to significant under-prediction of the

inundation extent. From the above three cases with various values of θ , it is clear that the inundation extent changes depending on the value of θ and the optimum value of θ falls between 0.85 and 0.90. It is therefore clear that the use of constant θ demands a trial procedure for better prediction of inundation map. Figures 5d and 5e show the inundation extents predicted by s-centered and s-upwind schemes, respectively. It can be observed from Figures 5d and 5e that the use of adaptive θ in the s-schemes leads to the realistic prediction of the inundation extent.

To gain a better understanding on the effect of the value of θ , the amount of diffusion at each interface along the x - and y -directions are plotted along with the corresponding velocities for both s-centered and s-upwind schemes (Figure 6). A comparison of the plots shows that the amounts of diffusion and corresponding velocity at a location vary in a similar pattern. For instance, the simulated velocity along the x -direction is relatively higher when compared to that along the y -direction (Figures 6b and 6d, and Figures 6f and 6h). This velocity pattern is consistent with the physical behavior as the water flows from upstream to downstream of the setup. Subsequently, more diffusion is introduced by the s-schemes (Figures 6a and 6e) along the x -direction compared to the y -direction (Figures 6c and 6g). On the floodplain F1, LISFLOOD-FP with $\theta < 0.90$ produced unphysical over-flooding. The over-flooding is caused by a high diffusion value (~ 0.20) along the y -direction. However, when the diffusion along the y -direction is less than 0.1, the unphysical flooding does not occur on F1 (Figures 5d and 5e). In case of s-schemes, the proposed adaptive θ automatically takes care of such variations in the diffusion based on local water depth and velocity. Therefore, it produces a realistic inundation extent. The F values of the LISFLOOD-FP and the proposed s-schemes are summarized in Table 1, from which it can be seen that the proposed s-schemes show good skill in predicting inundation extents due to the use of adaptive θ . It may therefore be concluded that the proposed s-schemes improves the accuracy of the model compared to LISFLOOD-FP.

In addition to inundation extent, water depths simulated using the optimal Manning's coefficient (i.e., $0.009 \text{ m}^{-1/3}\text{s}$ for LISFLOOD-FP and $0.01 \text{ m}^{-1/3}\text{s}$ for s-schemes) is also compared with observed depths in the river as well as over the floodplains. Inside the river, the LISFLOOD-FP for $\theta = 0.90$ show reasonably good agreement with the observed water depths (Figure 7) and for $\theta = 0.85$ and 0.95 the accuracy of the simulated water depths are reduced. In case of s-schemes, the results agree well with the observed water depths at most of the gauges. In contrast, the comparison of results from s-schemes and LISFLOOD-FP over the floodplain, show both under and over prediction (Figure 8) at different gauges. However, the LISFLOOD-FP significantly over and under predicts the inundation extents for $\theta = 0.85$ and 0.95 , respectively as discussed before. The water depths obtained using s-schemes fall between those of the LISFLOOD-FP for $\theta = 0.85$ and 0.90 . The accuracy of predicted water depths estimated through the root mean square errors (RMSE) are given in Table 2. From the RMSE values, it can also be confirmed that the accuracy of s-schemes is better than that of the LISFLOOD-FP.

Steady-state experimental flood caused by inflow of $0.098 \text{ m}^3/\text{s}$ in a set-up

The calibrated Manning's roughness values of 0.009 and 0.01 are used to further assess the performance of the LISFLOOD-FP and s-schemes, for reproducing the steady-state experimental flood caused by an inflow of $0.098 \text{ m}^3/\text{s}$. The simulated inundation extents of LISFLOOD-FP for $\theta = 0.85$, 0.90 and 0.95 , and the proposed s-schemes are compared with the observed map (Figure 9). For $\theta = 0.85$, the LISFLOOD-FP model (Figure 9a) over predicts the inundation extent on

floodplains F1, F3 and F5. The over prediction is unphysical and it is because of the high diffusion value as discussed before. For $\theta = 0.90$, the predicted inundation extent is closer to the observed map (Figure 9b). In case of $\theta = 0.95$, the LISFLOOD-FP model shows under-prediction of the inundation extent (Figure 9c) at the upstream of the floodplain F1 and downstream of floodplain F2. It can be observed from Figures 9d and 9e that the s-schemes produce inundation extents closer to those observed. The accuracy of inundation extents obtained by the LISFLOOD-FP model (for $\theta = 0.85, 0.90$ and 0.95) and proposed s-schemes are compared in Table 3. The fitness values of s-schemes, once again underlines the improved predictive ability of adaptive θ . To demonstrate the effect of a variation in θ , the amount of diffusion along the x - and y -directions are plotted along with the corresponding velocities for both s-centered and s-upwind schemes (Figure 10). The simulated velocity along the x -direction is relatively higher in comparison to that along the y -direction (Figures 10b and 10d, and Figures 10f and 10h). Subsequently, higher diffusion is introduced by the s-schemes (Figures 10a and 10e) along the x -direction than in the y -direction (Figures 10c and 10g). On the floodplain F5, LISFLOOD-FP with $\theta = 0.85$ produces unphysical over-flooding owing to a high diffusion value (~ 0.20) along the y -direction. On the floodplains F1 and F4, LISFLOOD-FP with $\theta = 0.95$ under-predicts the inundation extent due to low diffusion value (~ 0.05) along the y -direction. In the case of s-schemes, adaptive θ varies the optimal amount of diffusion (~ 0.10) spatially based on local water depth and velocity (Figures 10d and 10h). This test case reconfirms the improved accuracy of s-schemes compared to LISFLOOD-FP.

Figures 11 and 12 compare the simulated and observed water depths in the river as well as over the floodplains. The results of LISFLOOD-FP show closer prediction of water depth for $\theta = 0.9$, over and under prediction for $\theta = 0.85$ and 0.95 , respectively. It can be observed that water depth results from s-schemes match very well in most of the gauges inside the river. On the other hand, the simulated water depths of LISFLOOD-FP as well as s-schemes over the floodplain are either under predicted or over predicted when compared to the observed depths. Interestingly, the water depths simulated by the s-schemes fall closer to the observed depths in most of the gauges compared to those by the LISFLOOD-FP model. The RMSE error in Table 4 suggests that the s-schemes predict water depths better than the LISFLOOD-FP model.

The relative computation time with respect to the s-centered scheme are also summarized in Tables 1 and 3, from which it can be observed that the LISFLOOD-FP model with $\theta = 0.8$ and 0.9 takes at least 18 % more computational time compared to the s-schemes. The enhanced stability condition of the proposed s-schemes allows a larger time step which in turn this improves the overall computational efficiency. The accuracy of the proposed s-schemes is shown to be consistently better than LISFLOOD-FP. Therefore, it may be concluded that the proposed s-schemes will help in eliminating the trial and error process of selecting an optimal value of θ as well as improve the accuracy of predicting the inundation extent in relatively less computation time compared to LISFLOOD-FP.

5.3 Urban flood simulation in Glasgow, UK

This test case is simulated to demonstrate the improved stability and performance of the proposed adaptive θ for a field application in an urban environment. The area of Greenfield, a suburb of Glasgow, UK, is thus chosen as a benchmark test case for comparing the performance of 2D

numerical models for which DEM and other data is available (Hunter et al., 2008; Fewtrell et al., 2008). The flooding at this site has been observed in response to a heavy rainfall event in the upstream catchment. The study site consists of a densely populated urban area along two main streets and topologically complex minor road networks as shown in Figure 13. The extent of the rectangular domain is 970 m \times 400 m.

On July 30, 2002, the site experienced an episode of flooding due to heavy rainfall at the upstream catchment area ($\sim 5 \text{ km}^2$) of X0. The runoff from the upstream flows through a small stream and enters the culvert at location X0 near the north-east corner (shown in Figure 13a). Beyond this point, the stream runs underground throughout the entire site. The flow exceeding the carrying capacity of the culvert is spilled onto the nearby surface and then flows along the two main streets that are oriented in the east-west direction through points X2 and X3. After interacting with the complex building network and minor road networks, the water eventually converges and ponds in the low-lying area, i.e. the southern part of the domain.

The hydrograph reported in Hunter et al. (2008) is used to specify the inflow boundary condition. The values of this hydrograph are constructed from the volume of water exceeding the carrying capacity of the culvert based on the best interpretation of eyewitnesses and historical photographs. For this study, such a hydrograph is digitized and imposed as the point source boundary condition at X0 (Figure 13a). All external boundary conditions are closed with zero mass fluxes. Simulations are carried out using the combinations of 13 friction coefficients (Table 5) chosen from physically plausible range as reported in Hunter et al. (2008). To corroborate the results of the proposed s-schemes, water depth results reported in Hunter et al. (2008) for two diffusive models (JFLOW and LISFLOOD-FP diffusive version) and four different full 2D models (TUFLOW, DIVAST, DIVAST-TVD and TRENT) are used as reference solutions. The model like JFLOW (Bradbrook et al., 2004), LISFLOOD-FP (Hunter et al., 2005) use simplified versions 2D equations, specifically the diffusive wave formulation, for its numerical solution. The full 2D models TUFLOW (Syme, 1991) and DIVAST (Falconer, 1986) solve the SWEs by implicit schemes, while DIVAST-DVT (D-TVD) (Liang et al., 2006) and TRENT (Villanueva and Wright, 2006) use explicit schemes. These model results are considered as reference solutions for comparisons. Two different cases are simulated for the duration of 120 minutes. In the first case, the proposed s-schemes and LISFLOOD-FP (version 5.8.9) inertial model are simulated with a single set of friction coefficients $0.015 \text{ m}^{-1/3}\text{s}$ and $0.05 \text{ m}^{-1/3}\text{s}$ as reported in Hunter et al. (2008). In the second case, simulation is carried out using an ensemble of 13 friction coefficient (Table 5). These identical spatially distributed friction coefficients are chosen to differentiate two land-use classes such as vegetated areas and tarmac areas from the OS Mastermap^(R) data.

In the first case, the time series of water depth obtained using s-schemes and LISFLOOD-FP inertial model are compared at four points X1, X2, X3 and X4 (Figure 13). These representative points are chosen to understand the hydraulic conditions occurring in the computational domain. The excess water from the culvert at X0 moves simultaneously towards points X1 and X2. At the commencement of simulation, water accumulates rapidly at point X1 as it is closer to point X0. Subsequently, the accumulated water drains slowly as the simulation proceeds. It may be observed from Figure 14a that the water depth predicted by s-schemes as well as LISFLOOD-FP models are in good agreement with the reference solutions. Point X2 is located along one of the main streets and it receives water from a single direction (from east to west). This point represents the area of shallow water zone with high velocity over which the complete flood wave travels. The comparison of water depths at X2 as shown in Figure 14b implies that the result from proposed s-

upwind and s-centered schemes fall closer to reference solutions. In contrast, the LISFLOOD-FP inertial model produces oscillatory water depth despite using θ to remove oscillations. The oscillations are more when the value of $\theta = 0.8$ or 0.9 and are relatively less for $\theta = 0.7$. Thus the results obtained for $\theta = 0.7$ (at all four stations) are reported in this section. The constant value of $\theta = 0.7, 0.8$ or 0.9 is not able to vary the right amount diffusion required to avoid oscillations. As a result, the LISFLOOD-FP inertial model becomes unstable for this combination of friction coefficient and shallow water depth. Point X3 is located in the area where ponding takes place eventually after receiving water from both the main streets through points X1 and X4. Therefore, the water depth is relatively deep at this location than at other places. Figure 14c shows close agreement of water depth simulated using the proposed s-schemes with the reference solutions, whereas LISFLOOD-FP inertial model over-predicts the water depth with small numerical oscillations. Point X4 represents the zone of convergent flow as it receives water along the north-south direction as well. This point also experiences shallow water depth similar to point X2. The water depths are compared in Figure 14d and the results by s-schemes are again observed to be closer to the reference solutions. It is clear from the Figure 14 that the proposed s-schemes produce smooth solutions without any numerical oscillations though with the LISFLOOD-FP inertial model, such oscillations are encountered. The absolute maximum difference between the peak water depths is found to be ~ 2 cm and ~ 3 cm for s-upwind and s-centered schemes, respectively. The error is of the same order as the vertical error in the LiDAR DEM (RMSE of ~ 5 cm).

Figure 15 shows the maximum inundation extents predicted by the s-schemes and the 2D-model available in LISFLOOD-FP suite. The results from the 2D-model is considered as reference inundation map (Figure 20c) since there is no observed inundation map available. It can be observed that s-upwind scheme behaves somewhat similar to full 2D model, while s-centered scheme slightly under-predicts the extent towards the west side. Overall, inside the urban area both the s-schemes produce results similar to those of the full 2D model.

In the second case, a mini-ensemble simulation is carried out using all the 13 pairs of roughness coefficients (n_{road} and n_{veg}) that are provided in Table 5. These identical spatially distributed parameter pairs are defined based on the major classes of land-use. Parameter n_{veg} is varied between 0.015 (bare earth) and 0.075 (dense tall grass and shrubs) with the increment of 0.005. Parameter n_{road} is varied between 0.008 and 0.020 with an interval of 0.001. These parameter sets are considered here to understand the performance of the diffusion coefficient in simulating urban flood with low Manning's roughness values. The simulations are carried out for all 13 combinations using the LISFLOOD-FP inertial model with $\theta = 0.7, 0.8$ and 0.9 and s-schemes with adaptive θ . The best results obtained for $\theta = 0.7$ are used herein for comparative study. The results of LISFLOOD-FP inertial model are compared with the maximum and minimum water depths obtained from the reference solution of full 2D models (Figures 16-18). The results corresponding to simulation number 1, 7 and 13 (Table 5) are discussed for clarity. The red line indicates the maximum and minimum possible range of the results for different combinations of Manning's coefficient (Table 5) from full 2D models. The black, blue and green lines indicate the results corresponding to the simulation test sequence 1 (n_{road} : 0.008, n_{veg} : 0.015), 7 (n_{road} : 0.014, n_{veg} : 0.045) and 13 (n_{road} : 0.020, n_{veg} : 0.075), respectively. It can be observed from Figure 21 that the LISFLOOD-FP inertial model produces numerical oscillations especially at points X2 and X4. For simulation number 13, the oscillations are relatively less. However, the water depths are either under or over predicted. Although $\theta = 0.9$ produces smooth solutions for simulation number 13

the oscillations are more pronounced for other roughness combinations, i.e., for simulations 1 to 12.

Figures 17 and 18 show the comparison of water depths obtained using the proposed s-schemes with adaptive θ . It is quite clear from Figures 17 and 18 that s-schemes are able to produce smooth results for all 13 combinations of the friction coefficients. The predicted water depths are found to be more or less within the minimum and maximum water depths of full 2D models. The smooth solutions have achieved from the use of adaptive θ , which is able to vary the value of diffusion $(1-\theta)$ more accurately in removing the oscillations. The relative computation time of the LISFLOOD-FP model (for $\theta = 0.7$) and s-upwind scheme are 1.14 and 1.02 times more compared to s-centered scheme. This case demonstrates the accuracy, robustness and the ability of adaptive θ in s-schemes to produce oscillation free solutions.

Overall, it can therefore be concluded that the use of constant θ value based local inertial model LISFLOOD-FP still suffers from numerical instability. Interestingly, the proposed s-schemes with adaptive, predicts the water depth accurately and also removes the issue of numerical oscillations.

5.4 Case Study on Chennai floods in 2015, India

In order to investigate the applicability of the proposed adaptive θ based local-inertial model for simulating large-scale floods, a rapidly urbanizing ungauged basin (Adyar) is chosen. The basin comprises the Southern part of Chennai city, India. The study area, as shown in Figure 19, extends between the latitudes $12^{\circ}47'6''$ N and $13^{\circ}3'22''$ N and longitudes $79^{\circ}52'36''$ and E $80^{\circ}17'1''$ E. The upstream portion of the study area is dominated by shrub land and water bodies, while the lower areas are a part of the Chennai Metropolitan Area (CMA). The Adyar River makes entry into the city at Nandambakkam Bridge and flows through the densely populated CMA before discharging into Bay of Bengal. It remains dry for most of the year but swells during the months October – November, the period coinciding with North - East (NE) monsoon. The city of Chennai often comes under the grip of deep depressions and cyclones during the NE monsoon. Coupled with the intense precipitation during this period, the city's low-lying terrain (average elevation is ~ 6 m), inefficient drainage structures, poorly maintained river and estuary hamper drainage of flood waters into the sea creating recurrent massive floods. During all the flood events, the areas close to Adyar River are the worst affected. Chennai and its adjacent districts experienced devastating floods during November-December 2015 which caused enormous economic loss along with a death toll of more than 400 people (Nithila Devi et al., 2019). The city received multiple torrential rainfalls during November 8 - December 1, 2015. On December 1, extremely heavy rainfall (about 60 mm/hr) was recorded that was considered to be a one in hundred year return period (i.e. 0.01 annual exceedance probability) event. As a consequence of such an extreme event, most parts of the city were flooded and the area adjacent to Adyar River were worst affected. The applicability of the developed model can therefore be rigorously tested if such a massive flood can be simulated with reasonable accuracy. For this purpose, the hydrological model HEC-HMS is set up for the entire Adyar basin as shown in Figure 19, whereas the hydraulic models (inertial and HEC-RAS) are set up from the confluence point (marked by a red dot in Figure 19) between the canal from the Chembarambakkam reservoir and the Adyar River to the downstream boundary at Bay of Bengal. The hydraulic model domain is represented by the shaded portion in Figure 19.

The calibration and validation of HEC-HMS for the selected flood event is presented in Nithila Devi et al. (2019). The flood hydrograph obtained from HEC-HMS model at the confluence point

is applied as the inflow boundary condition to the hydraulic models. At the ocean side, the observed tidal variations (Narasimhan et al., 2016) are prescribed as the downstream boundary condition. The bathymetry of the river and floodplains is represented using a $10\text{ m} \times 10\text{ m}$ resolution digital elevation model (DEM). The flood event is also simulated using 2D hydraulic models HEC-RAS and TELEMAC for comparison. Two 2D models results are used to examine if there is any model uncertainty before considering their results as reference solutions in the absence of detailed measured data for this particular event. For HEC-RAS and local-inertial models, the $150\text{ km} \times 8.5\text{ km}$ model domain is discretized into square grids with cell size of $10\text{ m} \times 10\text{ m}$, whereas the same flow domain is discretized into 59800 triangles for the TELEMAC model. It may be noted that TELEMAC 2D can capture the channel alignment with high accuracy by employing unstructured grids. The single Manning's n values of 0.025, 0.030, 0.035, 0.040, and $0.045\text{ m}^{-1/3}\text{s}$ as in Nithila Devi et al. (2019) are used to understand the variations in the simulated results.

Flood depth comparison

For comparing the results of s-schemes, simulations are also carried out using the LISFLOOD-FP model and the 2D models. All the model results are compared with high flood water marks, which were surveyed soon after the flood by a team of researchers from various institutes such as IIT Madras, Anna University, National Institute of Ocean Technology (Chennai), and National Remote Sensing Centre (Hyderabad) using Differential Global Positioning System (DGPS) and digital point gauge. The accuracy of DGPS is of the order of $\pm 76\text{ mm}$ while that of the point gauge is $\pm 0.5\text{ mm}$. It should be noted that the measured data also involves certain amount of human error, which cannot be quantified (Fewtrell et al., 2011; Parkes et al., 2013). The hydraulic simulations are run from November 30 to December 3, 2015. The simulated and surveyed flood water-marks are compared in Figure 20. It is observed that for full 2D models, better results are obtained for Manning's n value of $0.035\text{ m}^{-1/3}\text{s}$ with the RMSE error of 0.52 and 0.54 m and coefficient of regression of 0.95 and 0.94 for HEC-RAS and TELEMAC models, respectively. The 2D models are found to maintain similar level of accuracy and hence the 2D model results can be used as reference solutions, especially time-series of water depth and maximum flood extent. On the other hand, s-schemes and LISFLOOD-FP are found to produce best results for Manning's n value of $0.040\text{ m}^{-1/3}\text{s}$. Also, LISFLOOD-FP is observed to be accurate for $\theta = 0.8$. Therefore, for full 2D and inertial models Manning's n values of $0.035\text{ m}^{-1/3}\text{s}$ and $0.040\text{ m}^{-1/3}\text{s}$ are considered as the calibrated values. It can also be observed (Figure 20) that both the s-schemes are able to simulate this flood event with the similar levels of accuracy, which are relatively better than LISLOOD-FP model.

Furthermore, to assess the accuracy of the proposed s-schemes, the time-series of water depths at selected locations (shown in Figure 19) are compared against LISFLOOD-FP, TELEMAC and HEC-RAS results (Figure 21). The water depth profiles obtained using inertial models are found to be closer to HEC-RAS results compared to TELEMAC. This might be due to the fact that the inertial models and HEC-RAS use the same computational grid, in addition the solution of HEC-RAS and TELEMAC models are also different. Hence, the accuracies of the local-inertial models is evaluated using water depths computed by HEC-RAS as reference solutions and are enlisted in Table 6 and 7. It can be observed from Table 6 that the proposed s-upwind scheme is able to predict the water depths better than s-centered scheme and LISFLOOD-FP. In terms of time to peak flood, all the inertial schemes show certain amount of delay (Table 7), among which the s-upwind scheme has lesser delay followed by the s-centered scheme and LISFLOOD-FP model. The delay might be due to the fact that the advection term is neglected in the momentum equation. Overall, it can

be concluded that the adaptive θ concept for local-inertial model is seen to improve the prediction of time-series of water depth in comparison to the LISFLOOD-FP model.

Comparison of flood extent

The maximum flood extent obtained by HEC-RAS is used as reference solution due to lack of observed inundation extent. For qualitative comparison, actual, under and over predicted areas are shown in three different colours in Figure 22. Figures 22a and 22b imply that the s-upwind and s-centered schemes predict inundation extent better than LISFLOOD-FP model (Figure 22c). Quantitative comparisons using the measure of fit function, F (equation 17) emphasize the same conclusion with the values of 94%, 90% and 86% for the proposed s-upwind and s-centered schemes and LISFLOOD-FP, respectively. The contour maps of maximum flood extent are plotted in Figure 23. The difference of maximum flood depth of HEC-RAS with s-schemes and LISFLOOD-FP is within ~ 0.5 m. Altogether the results imply that the local-inertial models can simulate a severe flood event with a level of accuracy similar to that of a full 2D model.

The relative computation time of the LISFLOOD-FP model is ~ 1.32 and ~ 1.37 times more than that of the proposed s-upwind and s-centered schemes, respectively, whereas, HEC-RAS 2D model takes ~ 26 times more computation time. Hence, it is clear that the proposed local-inertial model takes significantly less computation time compared to HEC-RAS 2D model. In addition, the proposed s-schemes improve the overall computation time by at least ~ 1.3 times compared to LISFLOOD-FP model. The computation time of inertial models can be reduced significantly through the implementation of parallel processing as described in the introduction.

6 Conclusions

This study focuses on the development of a rapid flood prediction model with minimum process representation. One such model developed by Bates et al. (2010) and improved by de Almeida et al. (2012) is used in many applications for large-scale flood simulations. For oscillation free solutions, de Almeida et al. (2012) introduced an artificial diffusion term through a weighting factor θ in the numerical schemes (termed as q-schemes). The value of θ controls the amount of diffusion and hence determines the flux diffusion through the cell boundaries. As a consequence, the accuracy of the q-schemes depends on the value of θ , which is considered to be an arbitrary constant value and requires repeated trials to arrive at its optimal value. To circumvent this problem, an explicit expression for θ is proposed in this study, where θ varies both spatially and temporally, being a function of velocity, water depth, grid and time step size. The proposed adaptive θ is implemented in the q-schemes proposed in de Almeida et al. (2012) and are termed as s-schemes in this study. The s-schemes are rigorously investigated by simulating the following test cases: (a) nonbreaking wave propagation over a horizontal plane, (b) nonbreaking wave propagation on a planar beach, (c) an experimental 2D steady flow in a river-network-floodplain setup, (d) an urban flood event in Glasgow, UK and (f) Chennai flood of 2015, India.

The analytical test cases indicate that the proposed s-schemes perform consistently better than q-schemes for different Manning's n values without numerical oscillations. Further, it is found that the accuracy of upwind scheme is influenced more by the value of weighting factor θ rather than the zero-th order term associated with the upwind scheme as reported in de Almeida et al. (2012). The simulation of the experimental set-up at IITM demonstrates that the usage of the same constant θ along both the x - and y -directions deteriorates the accuracies of predicted inundation extent and

inappropriate value of θ can produce nonphysical inundation extent. The proposed s-schemes predict the inundation extent accurately as it maintains the spatial and temporal variations of diffusion value using adaptive θ . The results from the simulation of the urban flood event in Glasgow, UK indicates that the q-schemes still sufferer from numerical instability despite the use of constant θ value, while the proposed s-scheme delivers smooth solutions for all considered combinations of low frictions. Finally, the large-scale simulation of the disastrous Chennai flood (2015) prove that the proposed s-schemes can simulate a severe flood event with accuracy similar to that of a full 2D model. Overall, the prosed s-schemes improve the model stability and accuracy.

The proposed s-schemes are also shown to be stable even at higher value of CFL = 0.9 compared to CFL = 0.8 used in LISFLOOD-FP. As a result, the proposed s-schemes not only improve the numerical stability but also enhances the computational efficiency. Again, q- as well as s-schemes are found to be significantly faster than the HEC-RAS 2D model (~ 25 times). The validation and application prove that the developed local-inertial model with adaptive θ has the potential to be used in a rapid flood prediction system.

The following specific conclusions are drawn from this study.

- i) A mathematical expression for adaptive θ is derived on the basis of water depth, velocity, grid and time step size. This explicit expression eliminates the trial and error procedure used so far in local-inertial models and also solves the problem on numerical instability. The expression can be used in both centered and upwind schemes of local-inertial models, which can be used for rapid large-scale flood prediction.
- ii) The rigorous validation and application clearly show that the developed s-schemes with adaptive θ improve the accuracy when compared to LISFLOOD-FP model for slow rising floods.
- iii) The adaptive θ is shown to allow the use of higher CFL value and hence overall computation time is reduced compared to LISFLOOD-FP and 2D models.
- iv) The proposed adaptive θ in the s-upwind scheme performs with almost the same accuracy and computation time as that of the s-centered scheme. Hence, the conclusion of de Almeida et al. (2012) that the performance of the upwind scheme is inconsistent is proven to be invalid.

7 Acknowledgements

This work was supported by the DST-SERB, India [grant number EMR/2017/000642]. Authors would like to thank Dr. Balaji Narasimhan for providing the DEM of the Adyar Basin. The experimental dataset (Dataset 3) observed in the river-network-floodplain setup is available here: <https://www.hydroshare.org/resource/e5a28a1c273641ff9d4b334fd2d06580/>.

References

- Aricò, C., Filianoti, P., Sinagra, M., & Tucciarelli, T. (2016). The FLO Diffusive 1D-2D Model for Simulation of River Flooding. *Water*, 8(5), 200. <https://doi.org/10.3390/w8050200>.
- Aronica, G., Bates, P. D. L., & Horritt, M. S. (2002). Assessing the uncertainty in distributed model predictions. *Hydrological Processes*, 2001–2016. <https://doi.org/10.1002/hyp.398>
- Aronica, G., Tucciarelli, T., & Nasello, C. (1998). 2D Multilevel Model for Flood Wave Propagation in Flood-Affected Areas. *Journal of Water Resources Planning and Management*, 124(4), 210–217. [https://doi.org/10.1061/\(ASCE\)0733-9496\(1998\)124:4\(210\)](https://doi.org/10.1061/(ASCE)0733-9496(1998)124:4(210)).
- Bates, P. D., & De Roo, A. P. J. (2000). A simple raster-based model for flood inundation simulation. *Journal of Hydrology*, 236(1–2), 54–77. [https://doi.org/10.1016/S0022-1694\(00\)00278-X](https://doi.org/10.1016/S0022-1694(00)00278-X).
- Bates, P. D., Wilson, M. D., Horritt, M. S., Mason, D. C., Holden, N., & Currie, A. (2006). Reach scale floodplain inundation dynamics observed using airborne synthetic aperture radar imagery : *Data analysis and modelling*, 306–318. <https://doi.org/10.1016/j.jhydrol.2005.12.028>.
- Bates, P. D., Horritt, M. S., & Fewtrell, T. J. (2010). A simple inertial formulation of the shallow water equations for efficient two-dimensional flood inundation modelling. *Journal of Hydrology*, 387(1–2), 33–45. <https://doi.org/10.1016/j.jhydrol.2010.03.027>.
- Baugh, C. A., Bates, P. D., Schumann, G., & Trigg, M. A. (2013). SRTM vegetation removal and hydrodynamic modeling accuracy. *Water Resources Research*, 49(9), 5276–5289. <https://doi.org/10.1002/wrcr.20412>.
- Bermudez, A., Rodriguez, C., & Vilar, M. A. (1991). Solving Shallow Water Equations by a Mixed Implicit Finite Element Method. *IMA Journal of Numerical Analysis*, 11(September 2014), 79–97. <https://doi.org/10.1093/imanum/11.1.79>.
- Bradbrook, K. F., Lane, S. N., Waller, S. G., & Bates, P. D. (2004). Two dimensional diffusion wave modelling of flood inundation using a simplified channel representation. *International Journal of River Basin Management*, 2(3), 211–223.
- Brown, J. D., Spencer, T., & Moeller, I. (2007). Modeling storm surge flooding of an urban area with particular reference to modeling uncertainties: A case study of Canvey Island, United Kingdom. *Water Resources Research*, 43(6), 1–22. <https://doi.org/10.1029/2005WR004597>.
- Brunner, G.W. (2016). HEC-RAS River Analysis System, Hydraulic Reference Manual (Version 5), US Army Corps of Engineers, Davis (2016).
- Bruwier, M., Archambeau, P., Erpicum, S., Piroton, M., & Dewals, B. (2017). Shallow-water models with anisotropic porosity and merging for flood modelling on Cartesian grids. *Journal of hydrology*, 554, 693–709.

858 Cea, L & Blade, E. (2015). A simple and efficient unstructured finite volume scheme for solving
859 the shallow water equations in overland flow applications. *Water Resources Research*, 5464–
860 5486. <https://doi.org/10.1002/2014WR016547>.

861 Coulthard, T. J., Neal, J. C., Bates, P. D., Ramirez, J., de Almeida, G. A. M., and Hancock, G. R.:
862 Integrating the LISFLOOD-FP 2D hydrodynamic model with the CAESAR model:
863 implications for modelling landscape evolution, *Earth Surf. Proc. Landf.*, 38, 1897–1906,
864 doi:10.1002/esp.3478, 2013.

865 de Almeida, G. A. M., Bates, P., Freer, J. E., & Souvignnet, M. (2012). Improving the stability of a
866 simple formulation of the shallow water equations for 2-D flood modeling. *Water Resources*
867 *Research*, 48(5), 1–14. <https://doi.org/10.1029/2011WR011570>.

868 de Almeida, G.A.M. & Bates, P.D. (2013). Applicability of the local-inertial approximation of the
869 shallow water equations to flood modelling. *Water Resources Research*, 49 (8), 4833–4844.
870 (10.1002/wrcr.20366).

871 de Paiva, R. C. D., Buarque, D. C., Collischonn, W., Bonnet, M. P., Frappart, F., Calmant, S., &
872 Bulhões Mendes, C. A. (2013). Large-scale hydrologic and hydrodynamic modeling of the
873 Amazon River basin. *Water Resources Research*, 49(3), 1226–1243.
874 <https://doi.org/10.1002/wrcr.20067>.

875 Dottori, F., & Todini, E. (2010). A 2D flood inundation model based on cellular automata
876 approach. In *XVIII International Conference on Water Resources CMWR*. Barcelona.

877 Falconer, R. A. (1986). Water quality simulation study of a natural harbor. *Journal of Waterway,*
878 *Port, Coastal, and Ocean Engineering*, 112(1), 15-34.

879 Fewtrell, T. J., J. C. Neal, P. D. Bates, & P. J. Harrison, (2011). Geometric and structural river
880 channel complexity and the prediction of urban inundation. *Hydrological Processes*, 25,
881 3173–3186.

882 Fewtrell, T., Bates, P.D., Horritt, M., & Hunter, N. (2008). Evaluating the effect of scale in flood
883 inundation modelling in urban environments. *Hydrological Processes*, 22, 5107–5118.
884 (10.1002/hyp.7148).

885 Guidolin, M., Chen, A. S., Ghimire, B., Keedwell, E. C., Djordjević, S., & Savić, D. A. (2016). A
886 weighted cellular automata 2D inundation model for rapid flood analysis. *Environmental*
887 *Modelling & Software*, 84, 378-394.

888 Hervouet, J.M. (2000). TELEMAC modelling system: An overview. *Hydrological*
889 *Process.* 14 pp. 2209-2210, 10.1002/1099-1085(200009)14:13<2209:AID-
890 HYP23>3.0.CO;2-6.

891 Horritt, M. S., & Bates, P. D. (2001). Effects of spatial resolution on a raster based model of Flood
892 flow, *Journal of Hydrology*, 253, 239-249.

893 Horritt, M., Bates, P., Fewtrell, T., Mason, D., & Wilson, M. (2010). Modelling the hydraulics of
894 the Carlisle 2005 flood event. *Proceedings of the Institution of Civil Engineers, Water*
895 *Management*, 163 (6), 273-281. (10.1680/wama.2010.163.6.273).

896 Hubbard, M. E. (1999). Multidimensional slope limiters for MUSCL-Type of Finite volume
897 schemes on unstructured grids. *Journal of Computational Physics*, 155, 54–74.
898 <https://doi.org/10.1006/jcph.1999.6329>.

- 899 Hunter, N. M., Bates, P. D., Neelz, S., Pender, G., Villanueva, I., & Wright, N. G. (2008).
 900 Benchmarking 2D hydraulic models for urban flooding. *Proceedings of the Institution of Civil*
 901 *Engineers - Water Management*, 161(1), 13–30.
 902 <https://doi.org/10.1680/wama.2008.161.1.13>.
- 903 Hunter, N. M., Horritt, M. S., Bates, P. D., Wilson, M. D., & Werner, M. G. F. (2005). An adaptive
 904 time step solution for raster-based storage cell modelling of floodplain inundation. *Advances*
 905 *in Water Resources*, 28(9), 975–991. <https://doi.org/10.1016/j.advwatres.2005.03.007>
- 906 Kalyanapu, A. J., Shankar, S., Pardyjak, E. R., Judi, D. R., & Burian, S. J. (2011). Environmental
 907 Modelling & Software Assessment of GPU computational enhancement to a 2D flood model.
 908 *Environmental Modelling and Software*, 26(8), 1009–1016.
 909 <https://doi.org/10.1016/j.envsoft.2011.02.014>.
- 910 Kuiry, S. N., Ding, Y., & Wang, S. S. Y. (2010). Modelling coastal barrier breaching flows with
 911 well-balanced shock-capturing technique. *Computers and Fluids*, 39(10), 2051–2068.
 912 <https://doi.org/10.1016/j.compfluid.2010.07.015>.
- 913 Kuiry, S. N., Pramanik, K., & Sen, D. (2008). Finite volume model for shallow water equations
 914 with improved treatment of source terms. *Journal of Hydraulic Engineering*, 134(2), 231–242.
- 915 Lamb, R., Crossley, M., & Waller, S. (2009). A fast two-dimensional floodplain inundation model.
 916 In *Proceedings of the Institution of Civil Engineers-Water Management* (Vol. 162, No. 6, pp.
 917 363–370). Thomas Telford Ltd.
- 918 Lewis, M., Bates, P., Horsburgh, K., & Schumann, G. (2013). A storm surge inundation model of
 919 the northern Bay of Bengal using publicly available data A Bay of Bengal Storm Surge
 920 Inundation Model, (January), 358–369. <https://doi.org/10.1002/qj.2040>.
- 921 Liang, D., Falconer, R. A., & Lin, B. (2006). Comparison between TVD-MacCormack and ADI-
 922 type solvers of the shallow water equations. *Advances in water resources*, 29(12), 1833–1845.
- 923 Liang, Q. (2010). Flood Simulation Using a Well-Balanced Shallow Flow Model, 136(September),
 924 669–675.
- 925 Mali, V. K., & Kuiry, S. N. (2018). Assessing the accuracy of high-resolution topographic data
 926 generated using freely available packages based on SfM-MVS approach. *Measurement*, 124,
 927 338–350. <https://doi.org/10.1016/j.measurement.2018.04.043>.
- 928 Mali, V. K., & Kuiry, S. N. (2019). Experimental and numerical study of flood in a river-network-
 929 floodplain set-up. *Journal of Hydraulic Research*, 1–19.
- 930 Martins, R., Leandro, J., & Djordjević, S. (2015). A well balanced Roe scheme for the local-inertial
 931 equations with an unstructured mesh. *Advances in Water Resources*, 83, 351–363.
 932 <https://doi.org/10.1016/j.advwatres.2015.07.007>
- 933 Narasimhan, B., Bhallamudi, S. M., Mondal, A., Ghosh, S., & Mujumdar, P. (2016). Chennai
 934 floods 2015: A rapid assessment. *Bangalore: Interdisciplinary Centre for Water Research,*
 935 *IISc. Retrieved from Http://Itra. Medialabasia. in/Img/Chennai% 20Floods-Rapid%*
 936 *20Assessment% 20Report-May, 2023(May), 202016*
- 937 Neal, J., Bates, P.D., Fewtrell, T., Hunter, N., Wilson, M., & Horritt, M. (2009). Distributed whole
 938 city water level measurements from the Carlisle 2005 urban flood event and comparison with

- hydraulic model simulations. *Journal of Hydrology*, 368, 42-55. (10.1016/j.jhydrol.2009.01.026).
- Neal, J., Fewtrell, T., & Trigg, M. (2009). Environmental Modelling & Software Parallelisation of storage cell flood models using OpenMP. *Environmental Modelling and Software*, 24(7), 872–877. <https://doi.org/10.1016/j.envsoft.2008.12.004>
- Neal, J., Schumann, G., & Bates, P. (2012). A subgrid channel model for simulating river hydraulics and floodplain inundation over large and data sparse areas. *Water Resources Research*, 48(11), 1–16. <https://doi.org/10.1029/2012WR012514>.
- Neal, J., Villanueva, I., Wright, N., Willis, T., Fewtrell, T., & Bates, P.D. (2012). How much physical complexity is needed to model flood inundation? *Hydrological Processes*, 26 (15), 2264-2282. (10.1002/hyp.8339).
- Néelz, S., & Pender, G. (2013). Benchmarking the latest generation of 2D hydraulic modelling packages. *Environment Agency, Horison House, Deanery Road, Bristol, BS1 9AH*.
- Nithila Devi . N., Sridharan, B., & Kuiry, S. N. (2019). Impact of urban sprawl on future fl ooding in Chennai city , India. *Journal of Hydrology*, 574(April), 486–496. <https://doi.org/10.1016/j.jhydrol.2019.04.041>.
- Pappenberger, F., Beven, K. J., Hunter, N. M., Bates, P. D., Gouweleeuw, B. T., Thielen, J., & de Roo, A. P. J. (2005). Cascading model uncertainty from medium range weather forecasts (10 days) through a rainfall-runoff model to flood inundation predictions within the European Flood Forecasting System (EFFS). *Hydrology and Earth System Sciences*, 9(4), 381–393. <https://doi.org/10.5194/hess-9-381-2005>.
- Parkes, B. L., Cloke, H. L., Pappenberger, F., Neal, J., & Demeritt, D. (2013). Reducing Inconsistencies in Point Observations of Maximum Flood Inundation Level, *Earth interactions*, 17(6). <https://doi.org/10.1175/2012EI000475.1>
- Pau, J. C., & Sanders, B. F. (2006). Performance of Parallel Implementations of an Explicit Finite-Volume Shallow-Water Model, *Journal of Computing in Civil Engineering*, 20(2), 99–110.
- Peraire, J., O., C. Zienkiewicz., & Morgan. K. (1986), Shallow water problems: A general explicit formulation, *Int. J. Num. Methods Eng.*, 22, 547–574.
- Ponce, V. M. (1990), Generalized diffusion wave equation with inertial effects, *Water Resources Research*, 26(5), 1099–1101.
- Ponce, V. M., R. M. Li., & Simons D. B. (1978), Applicability of kinematic and diffusion models, *Journal of Hydraulic Engineering*, 104, 353–360.
- Pontes, P.R.M., Fan, F.M., Fleischmann, A.S., de Paiva, R.C.D., Buarque, D.C., Siqueira, V.A., Jardim, P.F., Sorribas, M.V., & Collischonn, W. (2017). Environmental Modelling & Software MGB-IPH model for hydrological and hydraulic simulation of large fl oodplain river systems coupled with open source GIS, 94. <https://doi.org/10.1016/j.envsoft.2017.03.029>.
- Sampson, C.C., Fewtrell, T.J., Duncan, A., Shaad, K., Horritt, M.S., & Bates, P.D. (2012). Using terrestrial laser scanning data to drive decimetric resolution urban inundation models. *Advances in Water Resources*, 41, 1-17. (10.1016/j.advwatres.2012.02.010).
- Sanders, B. F., Schubert, J. E., & Gallegos, H. A. (2008). Integral formulation of shallow-water

equations with anisotropic porosity for urban flood modeling. *Journal of Hydrology*, 362(1–2), 19–38. <https://doi.org/10.1016/j.jhydrol.2008.08.009>.

Sanyal, J., Carbonneau, P., & Densmore, A. L. (2013). Hydraulic routing of extreme floods in a large ungauged river and the estimation of associated uncertainties: A case study of the Damodar River, India. *Natural Hazards*, 66(2), 1153–1177. <https://doi.org/10.1007/s11069-012-0540-7>.

Shustikova, I., Domeneghetti, A., Neal, J. C., Bates, P., & Castellarin, A. (2019). Comparing 2D capabilities of HEC-RAS and LISFLOOD-FP on complex topography. *Hydrological Sciences Journal*, 64(14), 1769-1782.

Seyoum, S. D., Vojinovic, Z., Price, R. K., & Weesakul, S. (2012). Coupled 1D and Noninertia 2D Flood Inundation Model for Simulation of Urban Flooding, 138(January), 23–34. [https://doi.org/10.1061/\(ASCE\)HY.1943-7900](https://doi.org/10.1061/(ASCE)HY.1943-7900).

Syme, W. J. (1991). Dynamically Linked Two-dimensional/One-dimensional Hydrodynamic Modelling Program for Rivers, Estuaries & Coastal Waters. MEngSc thesis, University of Queensland, Australia.

Toro, E. F. (2001). *Shock-capturing methods for free-surface shallow flows*, Wiley, New York.

Villanueva, I., & Wright, N. G. (2006). Linking Riemann and storage cell models for flood prediction. In *Proceedings of the Institution of Civil Engineers-Water Management* (Vol. 159, No. 1, pp. 27-33). Thomas Telford Ltd.

Xia, R. (1994), Impact of coefficients in momentum equation on selection of inertial models, *Journal of Hydraulic Research*, 32, 615–621.

Yamazaki, D., de Almeida, G. A., & Bates, P. D. (2013). Improving computational efficiency in global river models by implementing the local inertial flow equation and a vector-based river network map. *Water Resources Research*, 49(11), 7221-7235.

Yan, K., Papenberger, F., Umer, Y. M., Solomatine, D. P., & Baldassarre, G. D. I. (2014). Regional versus physically-based methods for flood inundation modelling in data scarce areas: an application to the Blue Nile. *11th International Conference on Hydroinformatics - HIC 2014*.

Ying, X., Khan, A. A., & Wang, S. S. Y. (2004). Upwind Conservative Scheme for the Saint Venant Equations. *Journal of Hydraulic Engineering*, 130(10), 977–987. [https://doi.org/10.1061/\(ASCE\)0733-9429\(2004\)130:10\(977\)](https://doi.org/10.1061/(ASCE)0733-9429(2004)130:10(977)).

Yu, D., & Lane, S. N. (2011). Interactions between subgrid-scale resolution, feature representation and grid-scale resolution in flood inundation modelling. *Hydrological Processes*, 25(1), 36-53.

Table 1. Comparison of inundation fitness and computation time of inertial schemes for 0.078

Schemes	m ³ /s	
	Fitness (%)	Relative computation time
s-upwind	86	1.02
s-centered	84	1.00
LISFLOOD-FP ($\theta = 0.85$)	66	1.19
LISFLOOD-FP ($\theta = 0.90$)	76	1.17
LISFLOOD-FP ($\theta = 0.95$)	56	1.15

Table 2. RMSE (m) of water surface elevation of s-scheme and LISFLOOD-FP model for 0.078

Schemes	m ³ /s	
	River	Flood plain
s-upwind	0.83	0.70
s-centered	0.98	0.76
LISFLOOD-FP ($\theta = 0.85$)	1.68	2.60
LISFLOOD-FP ($\theta = 0.90$)	1.08	0.91
LISFLOOD-FP ($\theta = 0.95$)	1.23	2.52

Table 3. Comparison of fitness values for inundation extent and computation times of inertial schemes for 0.098 m³/s

Schemes	Fitness (%)	Relative computation time
s-upwind	92	1.03
s-centered	89	1.00
LISFLOOD-FP ($\theta = 0.85$)	87	1.21

LISFLOOD-FP ($\theta = 0.90$)	82	1.18
LISFLOOD-FP ($\theta = 0.95$)	79	1.14

Table 4. RMSE (m) of water surface elevation of s-scheme and LISFLOOD-FP model for 0.098 m³/s

Schemes	River	Flood plain
s-upwind	0.73	0.81
s-centered	0.72	1.02
LISFLOOD-FP ($\theta = 0.85$)	1.03	0.99
LISFLOOD-FP ($\theta = 0.90$)	0.76	1.35
LISFLOOD-FP ($\theta = 0.95$)	1.22	1.82

Table 5. Friction coefficient values used for the second case

Simulation No.	n_{road}	n_{veg}
1	0.008	0.015
2	0.009	0.020
3	0.010	0.025
4	0.011	0.030
5	0.012	0.035
6	0.013	0.040
7	0.014	0.045
8	0.015	0.050
9	0.016	0.055
10	0.017	0.060
11	0.018	0.065
12	0.019	0.070
13	0.020	0.075

Table 6. Comparison of errors in peak water depth with respect to HEC-RAS solutions

Schemes	Error in peak water depth (m)					
	Gauge 1	Gauge 2	Gauge 3	Gauge 4	Gauge 5	Gauge 6
s-upwind	0.007	0.198	0.231	-0.020	-0.055	-0.031
s-centered	0.258	0.467	0.547	-0.422	0.154	0.153
LISFLOOD-FP ($\theta = 0.8$)	0.411	0.619	0.649	-0.280	0.308	0.177

Table 7. Comparison of errors in time to peak flood with respect to HEC-RAS solutions

Schemes	Error in time to peak flood (min)					
	Gauge 1	Gauge 2	Gauge 3	Gauge 4	Gauge 5	Gauge 6
s-upwind	-27	-2	-32	-16	-16	-1
s-centered	-35	-17	-35	-28	-20	-8
LISFLOOD-FP ($\theta = 0.8$)	-40	-19	-36	-34	-26	-12

Figure Captions

Figure 1. Grid and variables used in the numerical scheme.

Figure 2. Diffusion and velocity profile obtained by the proposed s-schemes at $t = 2700, 5400$, and 9000 s for (e) 0.01 and (f) $0.005 \text{ m}^{-1/3}\text{s}$.

Figure 3. Predicted water surface elevation at $t = 1080, 2160, 2800$ and 3600 s using a uniform Manning coefficient of (a) 0.03 and (b) $0.01 \text{ m}^{-1/3}\text{s}$; (c) and (d) are the zoomed-in view of (a) and (b) at $t = 3600$ s.

Figure 4. IITM physical model setup showing the observation locations in the river and over the floodplain.

Figure 5. Comparison of simulated and observed inundation extent maps for LISFLOOD with $\theta =$ (a) 0.85 , (b) 0.90 , (c) 0.95 , (d) s-centered scheme and (e) s-upwind scheme for the steady-state discharge of $0.078 \text{ m}^3/\text{s}$.

Figure 6. Diffusion and velocity dependence for s-upwind scheme: along x -direction (a) diffusion, (b) velocity and along y -direction (c) diffusion and (d) velocity. Diffusion and velocity dependence for s-centered scheme: along x -direction (a) diffusion, (b) velocity and along y -direction (c) diffusion and (d) velocity.

Figure 7. Comparison of simulated and observed water depths in the river branches.

Figure 8. Comparison of simulated and observed water depth over floodplains

Figure 9. Comparison of simulated and observed inundation extent maps for LISFLOOD with (a) $\theta=0.85$, (b) $\theta=0.90$, (c) 0.95 , (d) s-centered scheme and (e) s-upwind scheme for the steady-state discharge of $0.098 \text{ m}^3/\text{s}$.

Figure 10. Diffusion and velocity dependence for s-upwind scheme: along x -direction (a) diffusion, (b) velocity and along y -direction (c) diffusion and (d) velocity.

Figure 11. Comparison of simulated and observed water depths in the river branches.

Figure 12. Comparison of simulated and observed water depth over floodplains

Figure 13. The Greenfield study site in Glasgow, UK (a) building and road network and (b) aerial photograph.

Figure 14. Comparison of water depths at stations (a) X1 (b) X2, (c) X3 and X4.

Figure 15. Comparison of inundation extents predicted by (a) s-upwind, (b) s-centered scheme with (c) full 2D model available in LISFLOOD-FP suite.

Figure 16. Water depth time series simulated using LISFLOOD-FP inertial model at (a) X1 (b) X2, (c) X3 and X4 for simulation no 1, 7 and 13 in Table 5.

Figure 17. Water depth time series simulated using s-upwind scheme at (a) X1 (b) X2, (c) X3 and X4 for the ensample of Manning's roughness coefficients provided in Table 5.

Figure 18. Water depth time series simulated using s-centered scheme at (a) X1 (b) X2, (c) X3 and X4 for the ensample of Manning's roughness coefficients provided in Table 5.

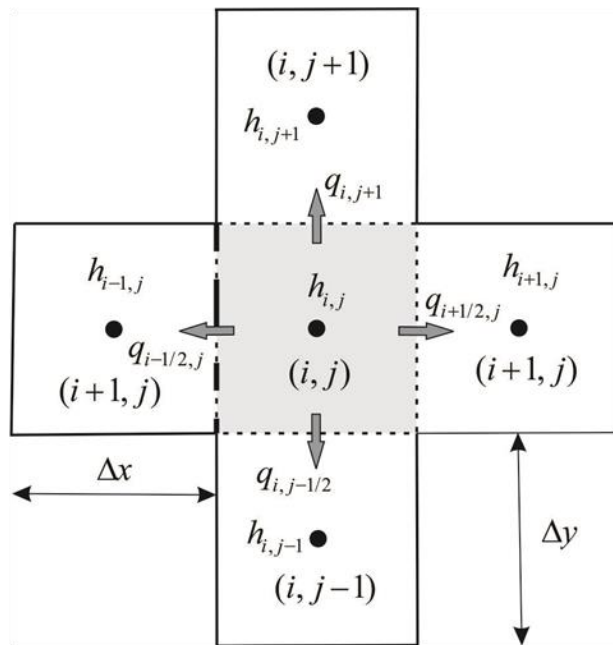
Figure 19. Map of the study area, Adyar basin. The red dot and the pink line indicate the location where the upstream and downstream boundary conditions, respectively are specified. Green dots indicate the locations where the time-series of water depth are compared.

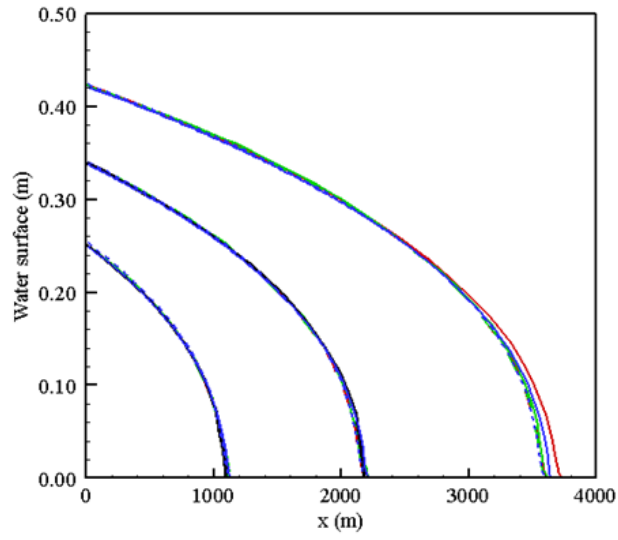
Figure 20. Scatter plot of simulated vs. observed maximum flood depths for 2015 flood in Chennai city.

Figure 21: Comparison of time-series of water depth at (a) Gauge 1, (b) Gauge 2, (c) Gauge 3, (d) Gauge 4, (e) Gauge 5 and (f) Gauge 6.

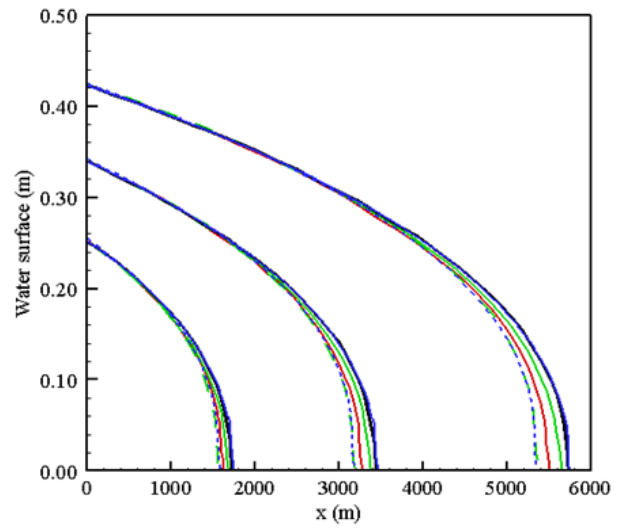
Figure 22: The maximum flood extent predicted by (a) s-upwind, (b) s-centered and (c) LISFLOOD-FP.

Figure 23: The maximum flood extent predicted by (a) HEC-RAS, (b) s-upwind, (c) s-centered and (d) LISFLOOD-FP.

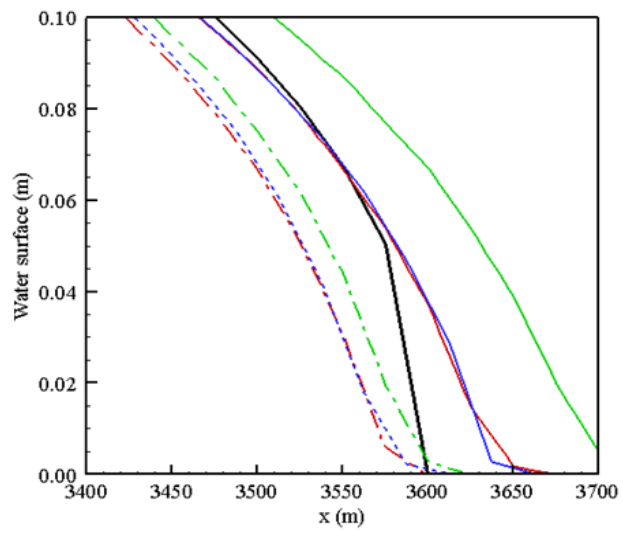




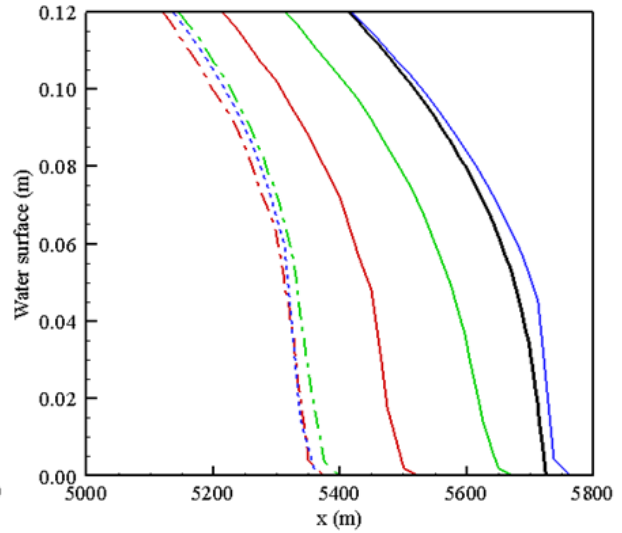
(a)



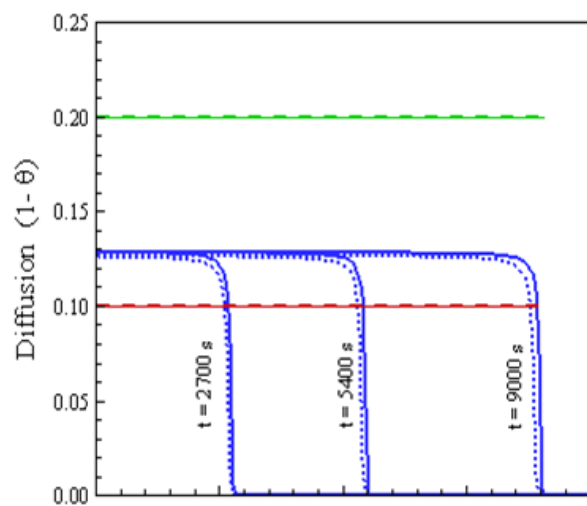
(b)



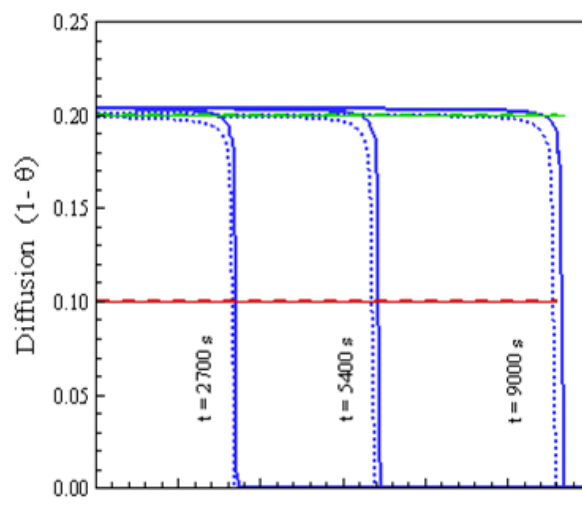
(c)



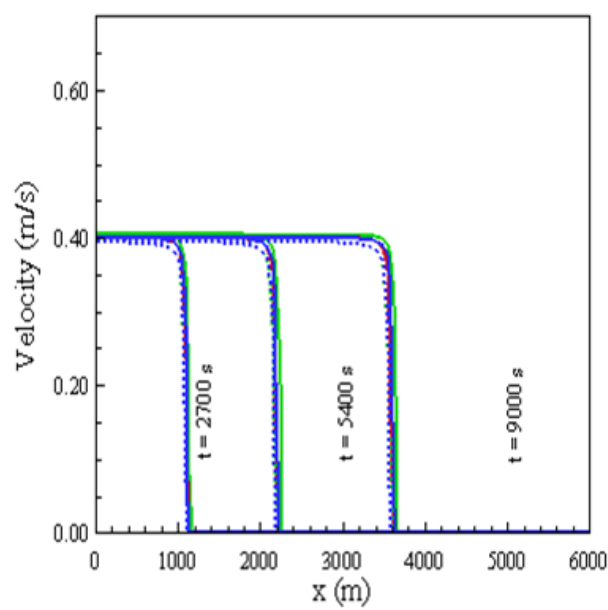
(d)



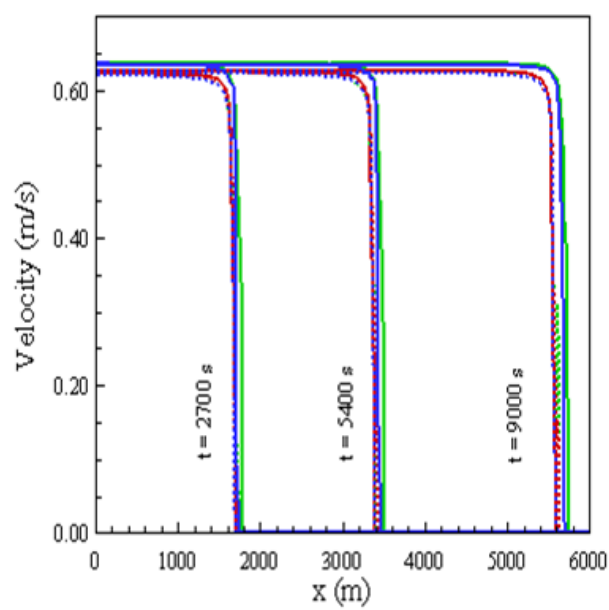
(e)



(f)



(g)



(h)

— Analytical

... s-centered

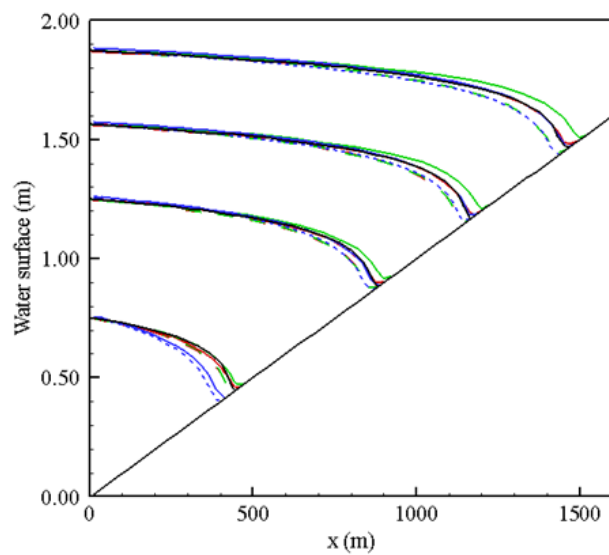
- - - q-centered ($\theta = 0.8$)

— q-upwind ($\theta = 0.8$)

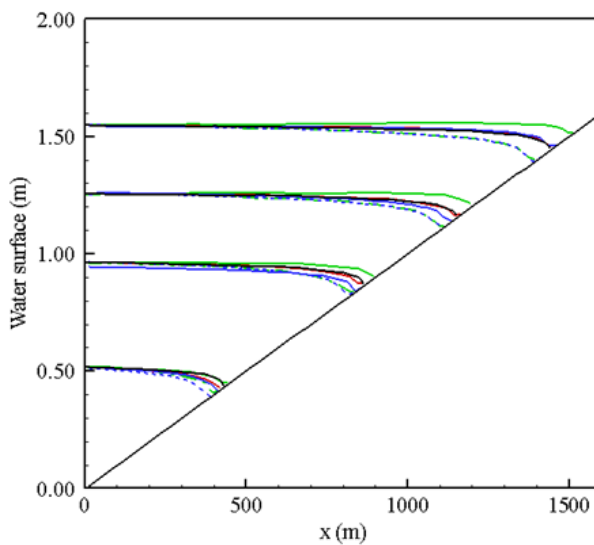
— s-upwind

- - - q-centered ($\theta = 0.9$)

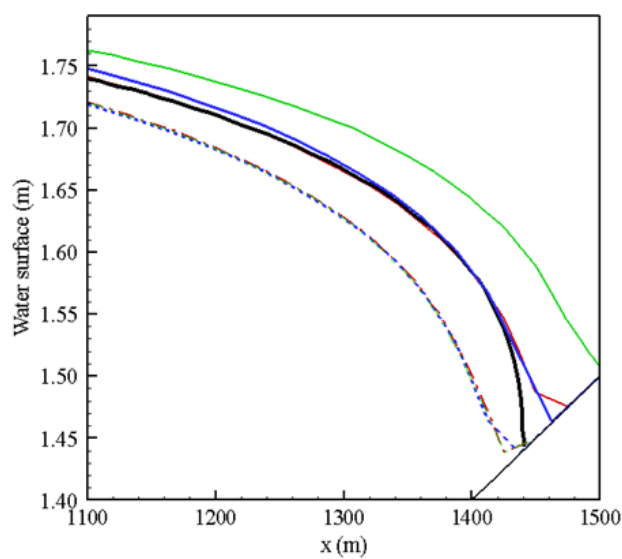
— q-upwind ($\theta = 0.9$)



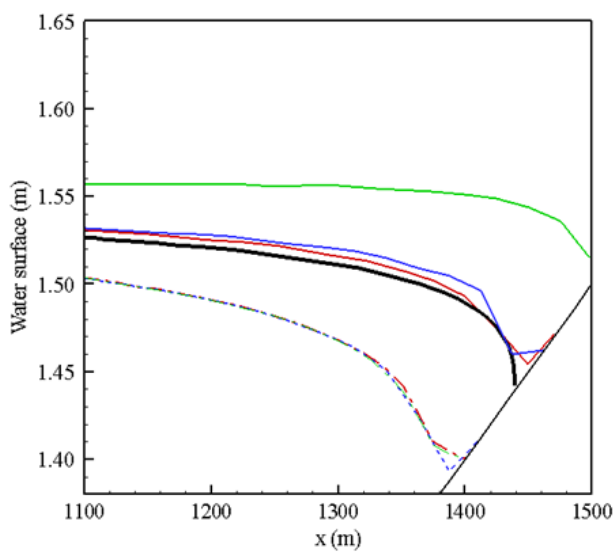
(a)



(b)



(c)



(d)

— Runge-Kutta

... s-centered

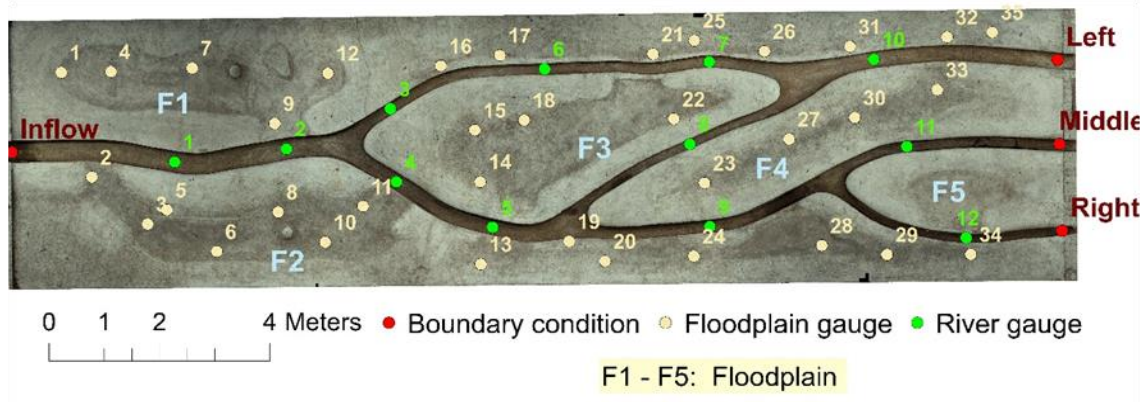
- - q-centered ($\theta = 0.8$)

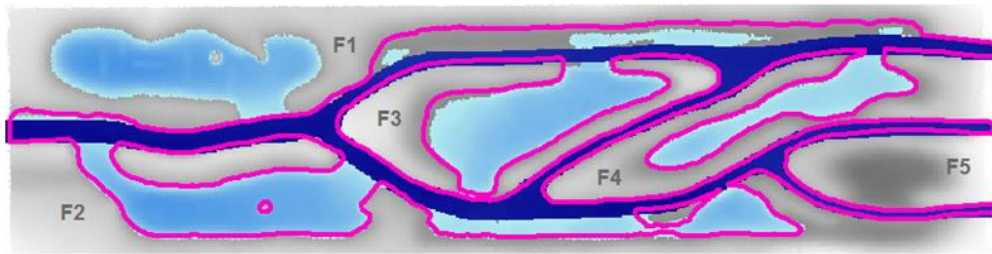
— q-upwind ($\theta = 0.8$)

— s-upwind

- - q-centered ($\theta = 0.9$)

— q-upwind ($\theta = 0.9$)

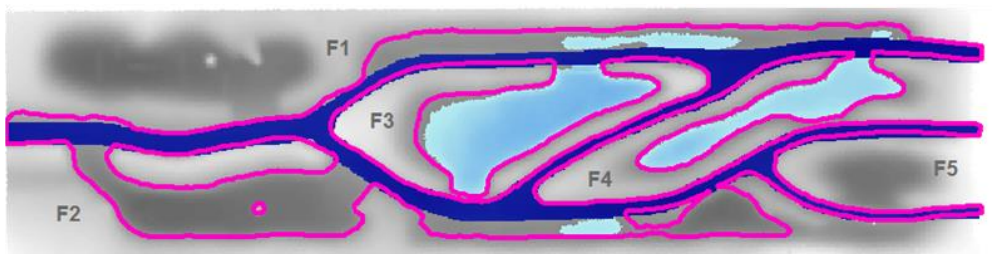




(a)



(b)



(c)



(d)



(e)



(a)



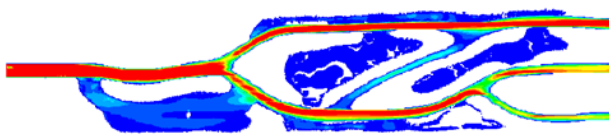
(b)



(c)



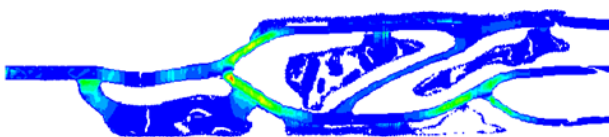
(d)



(e)



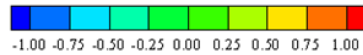
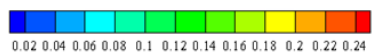
(f)

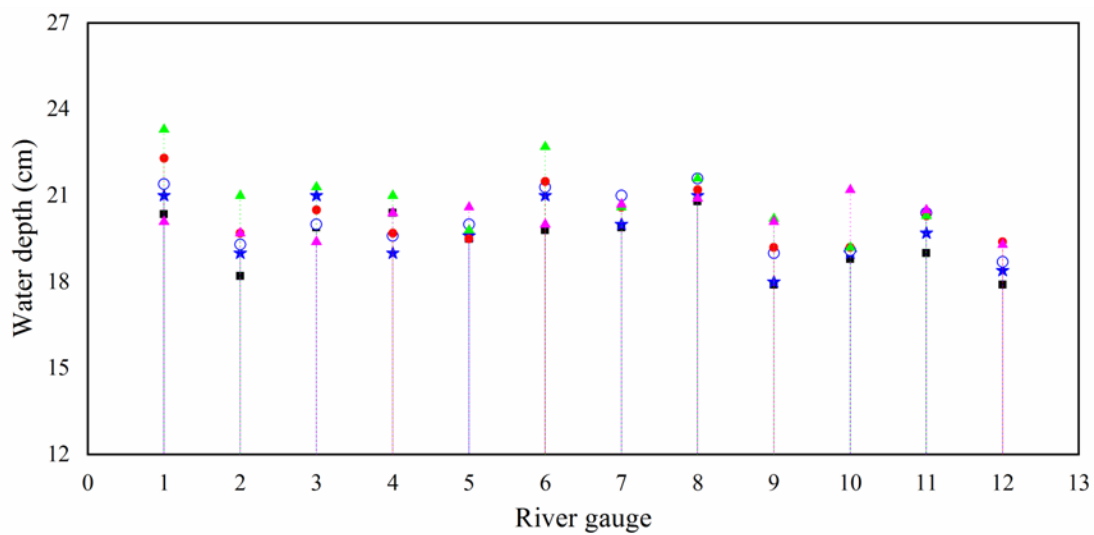


(g)



(h)



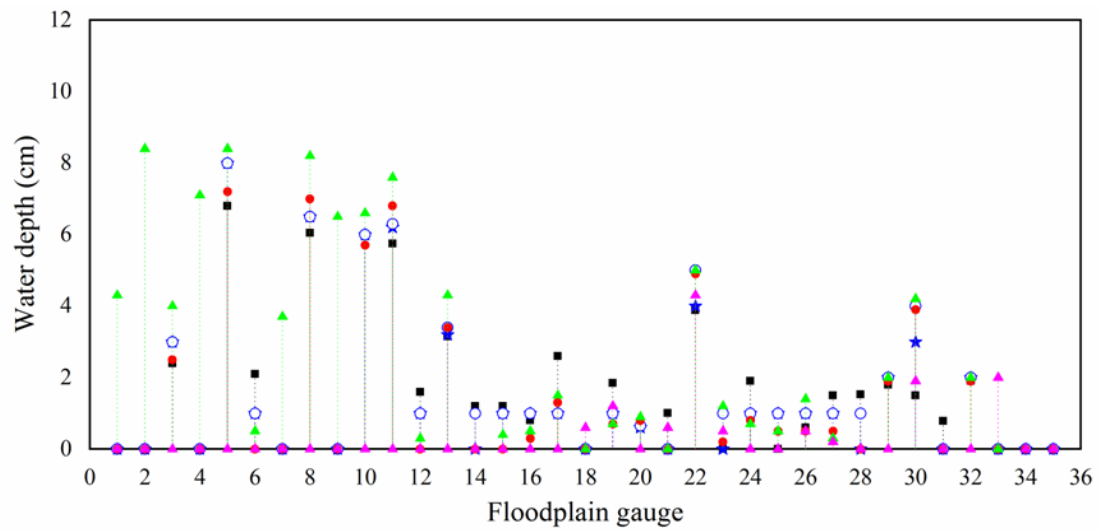


■ Observed

★ s-upwind

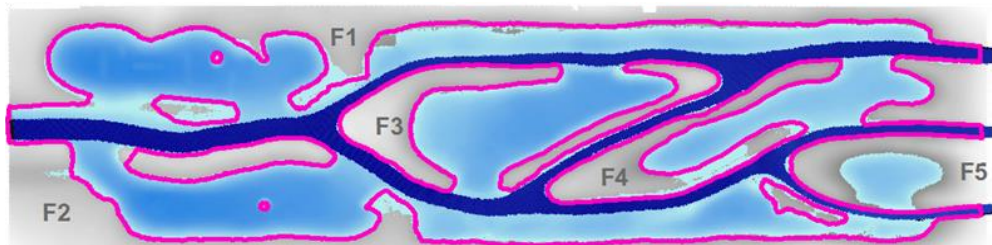
○ s-centered

▲ LISFLOOD-FP ($\theta=0.85$) ● LISFLOOD-FP ($\theta=0.90$) ▲ LISFLOOD-FP ($\theta=0.95$)

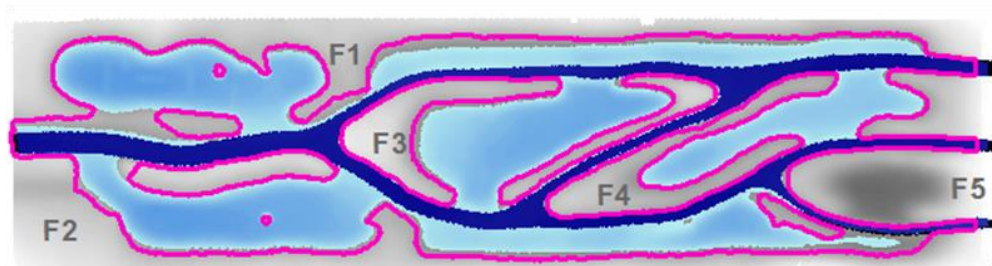


■ Observed ★ s-upwind ○ s-centered

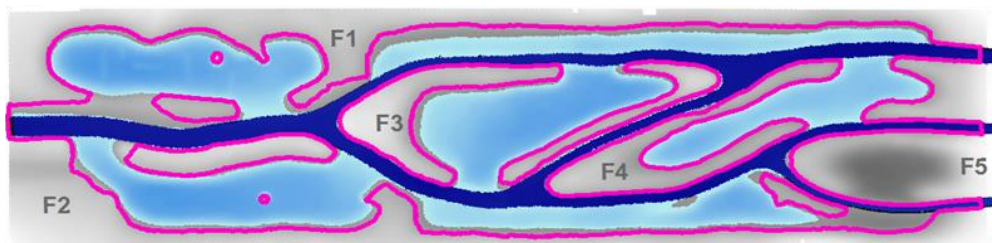
▲ LISFLOOD-FP ($\theta=0.85$) ● LISFLOOD-FP ($\theta=0.90$) ▲ LISFLOOD-FP ($\theta=0.95$)



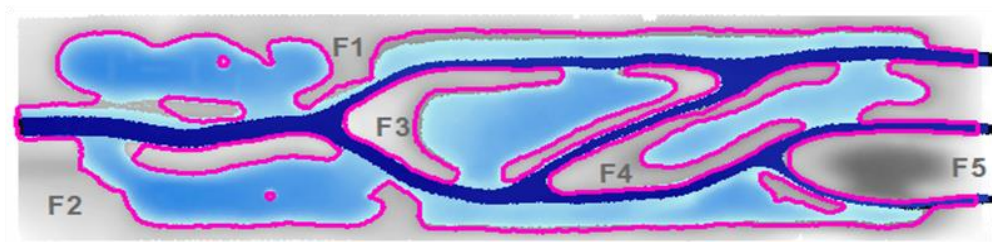
(a)



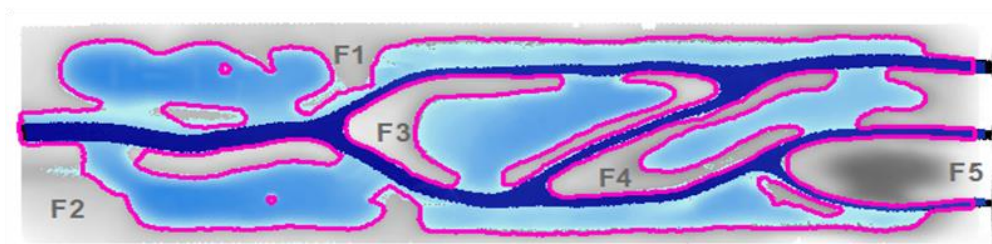
(b)



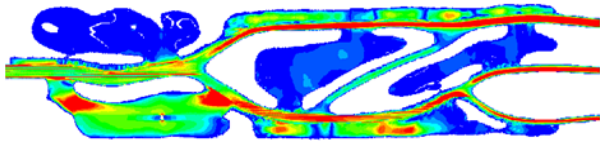
(c)



(d)



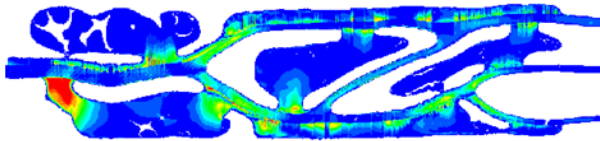
(e)



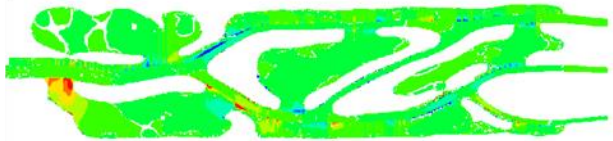
(a)



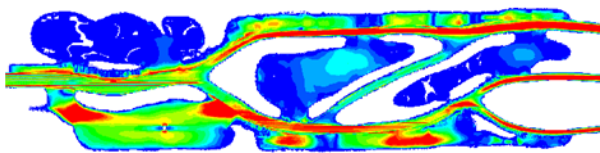
(b)



(c)



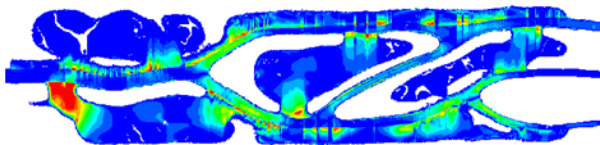
(d)



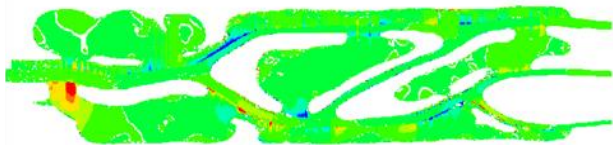
(e)



(f)

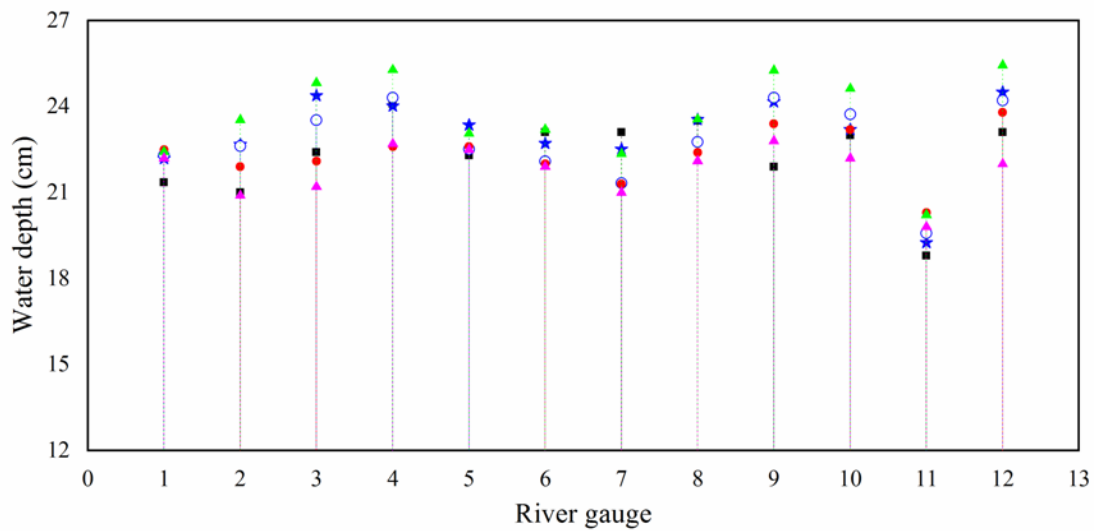


(g)



(h)



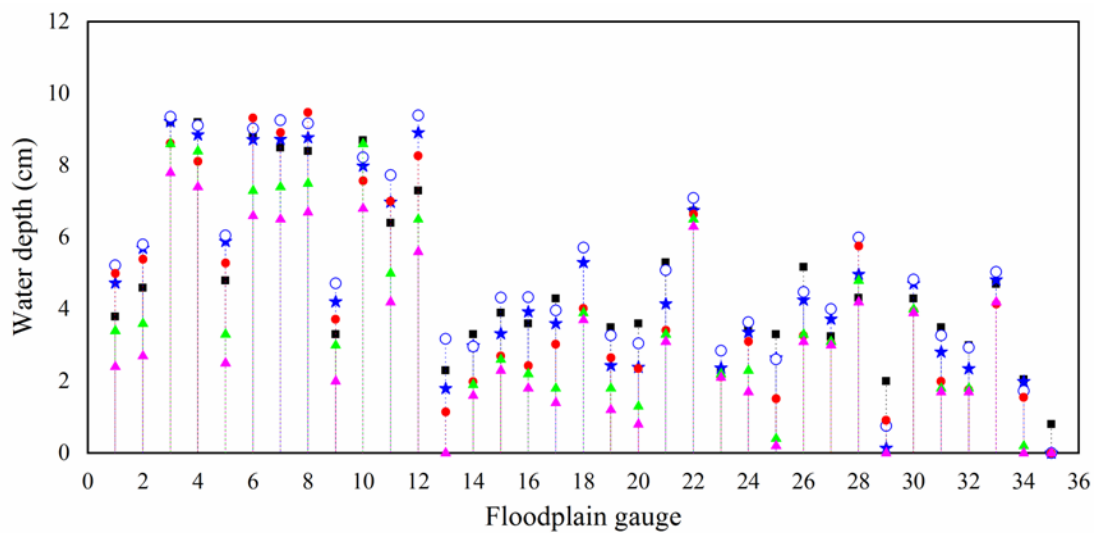


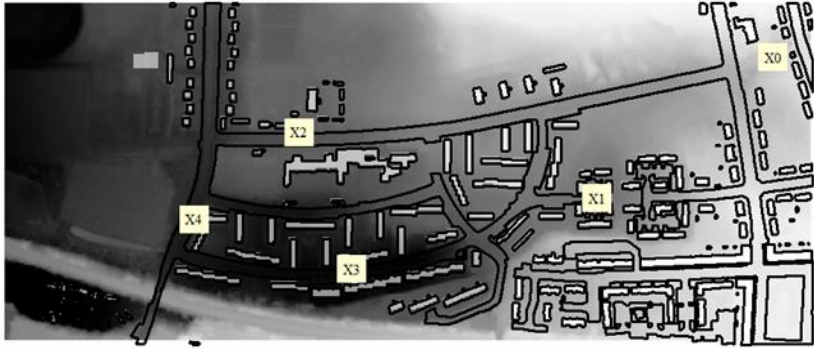
■ Observed

★ s-upwind

○ s-centered

▲ LISFLOOD-FP ($\theta=0.85$) ● LISFLOOD-FP ($\theta=0.90$) ▲ LISFLOOD-FP ($\theta=0.95$)

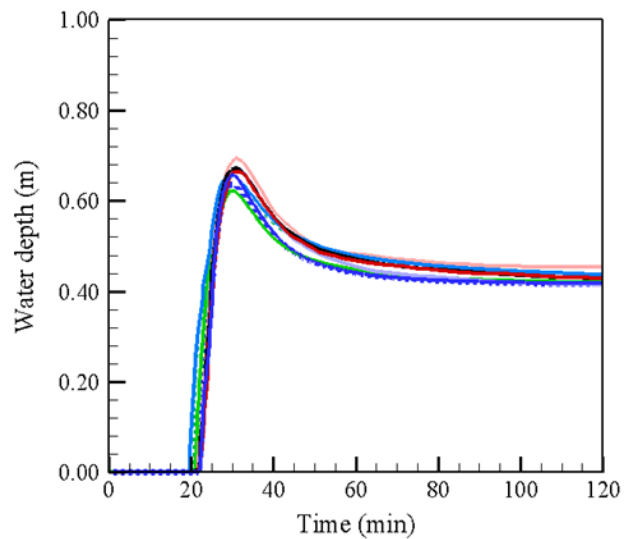




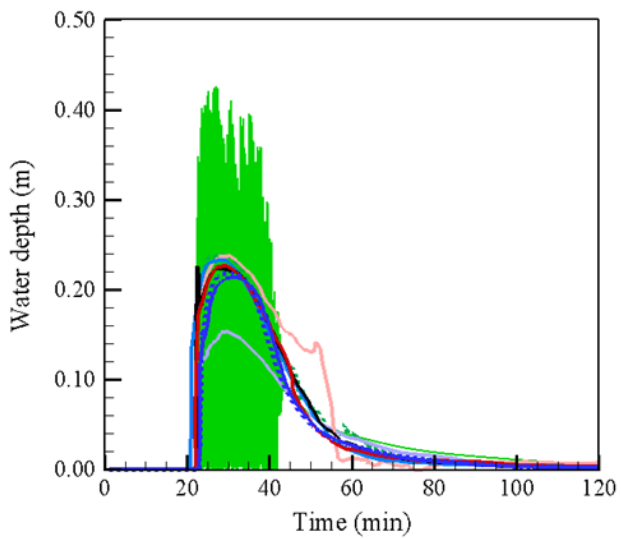
(a)



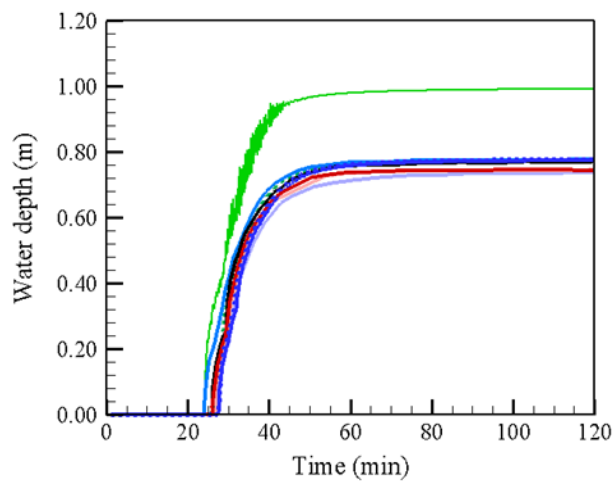
(b)



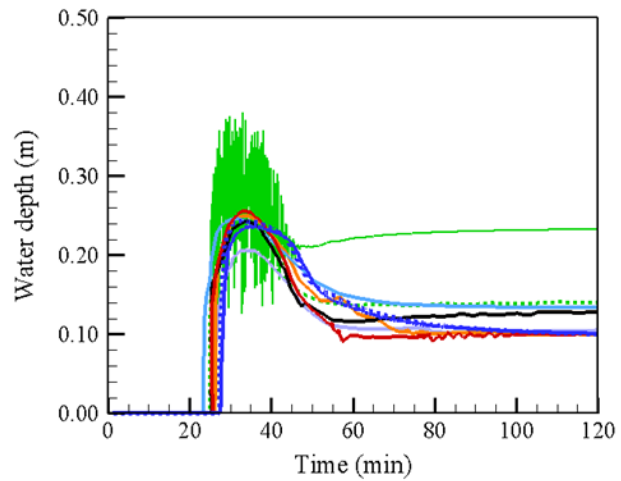
(a)



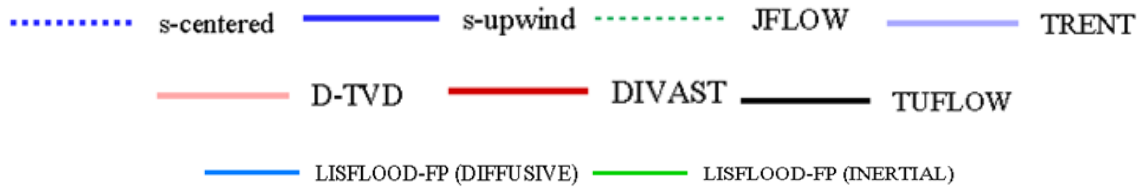
(b)

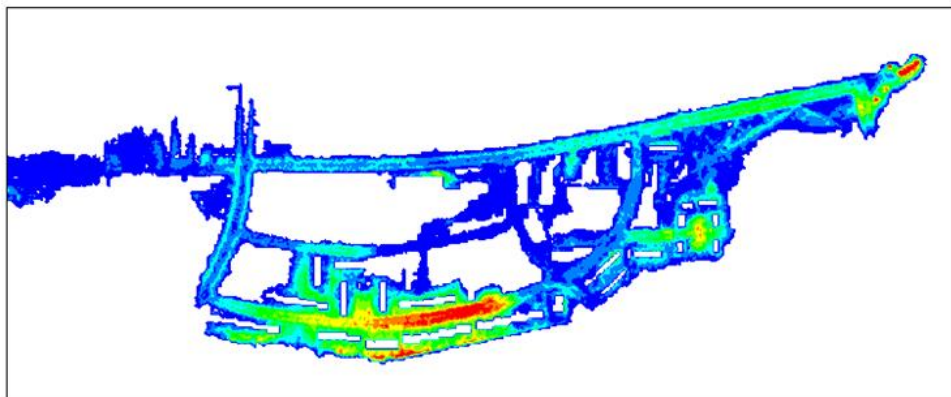


(c)

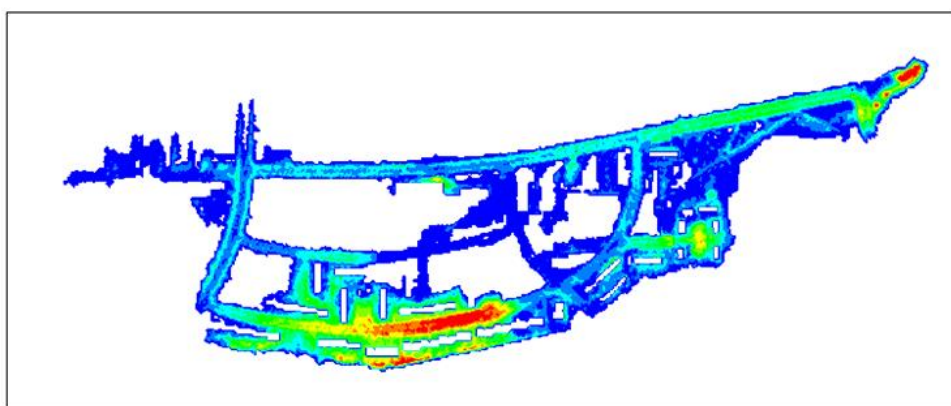


(d)

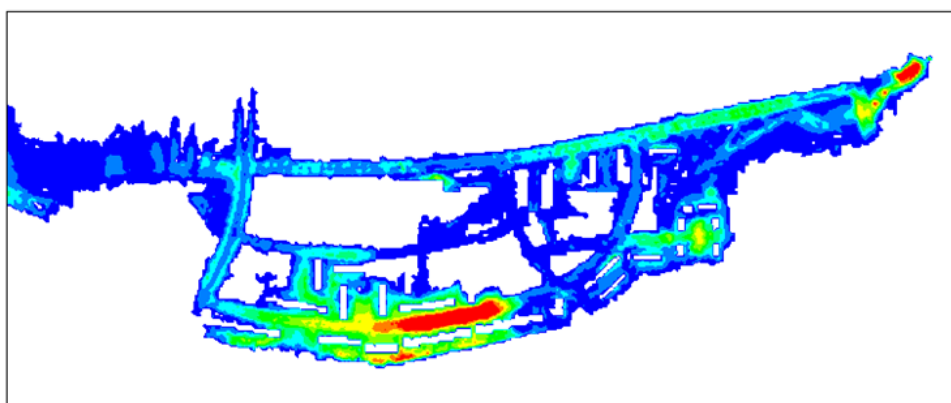




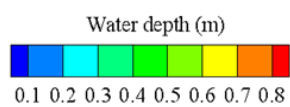
(a)

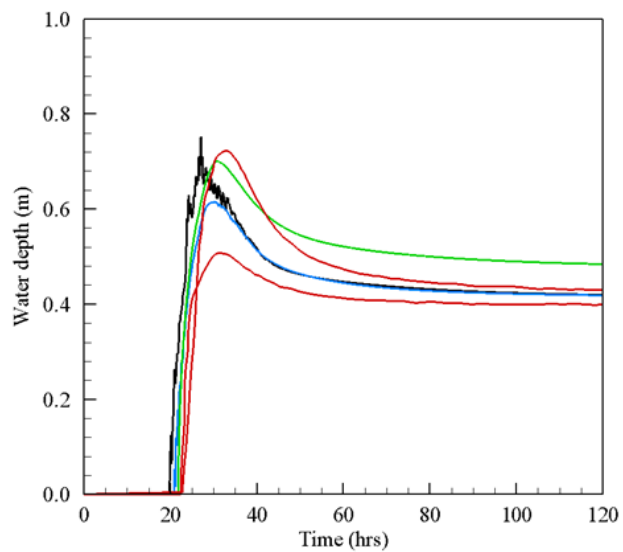


(b)

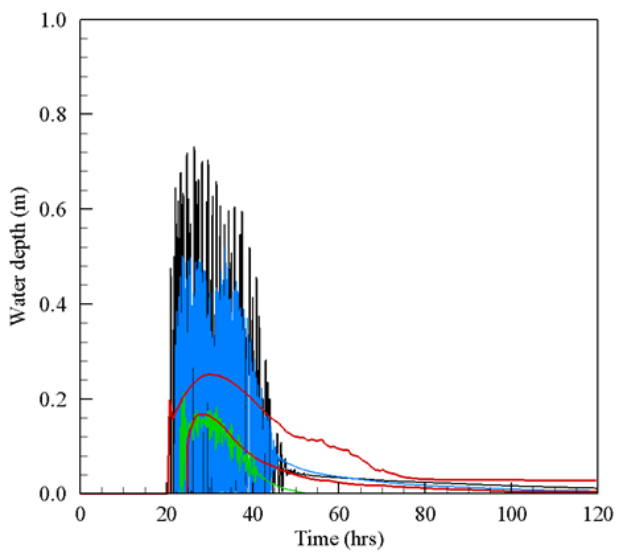


(c)

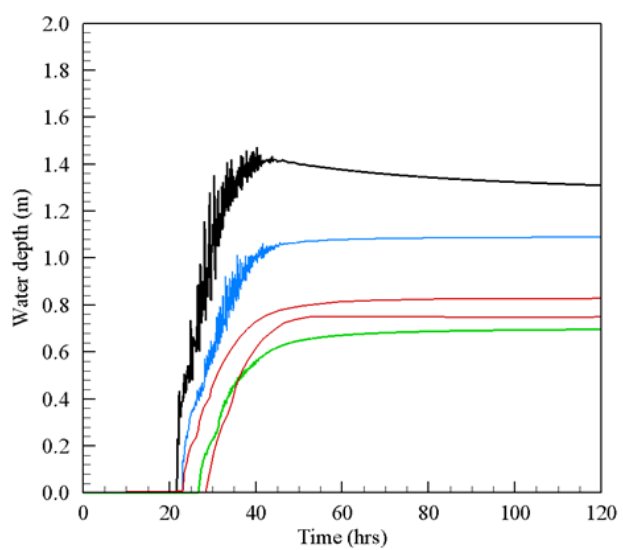




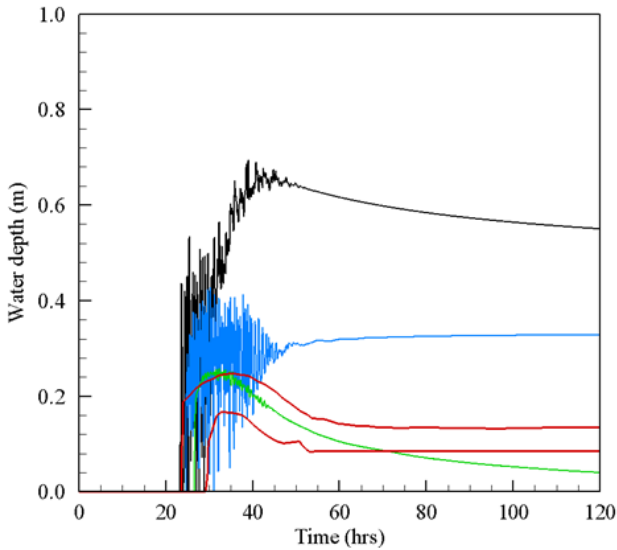
(a)



(b)

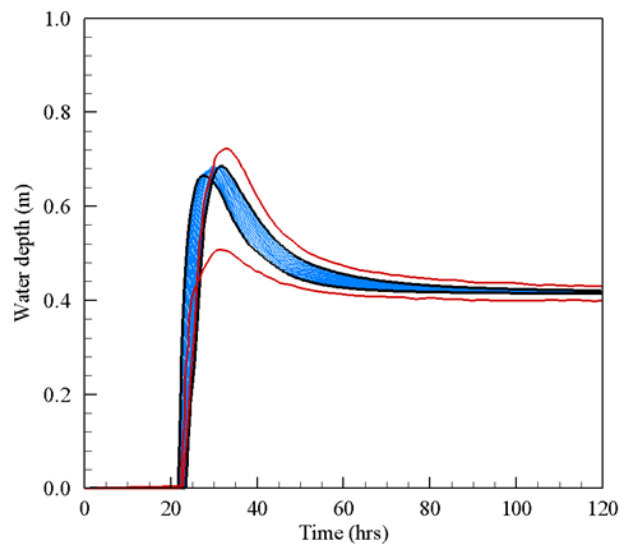


(c)

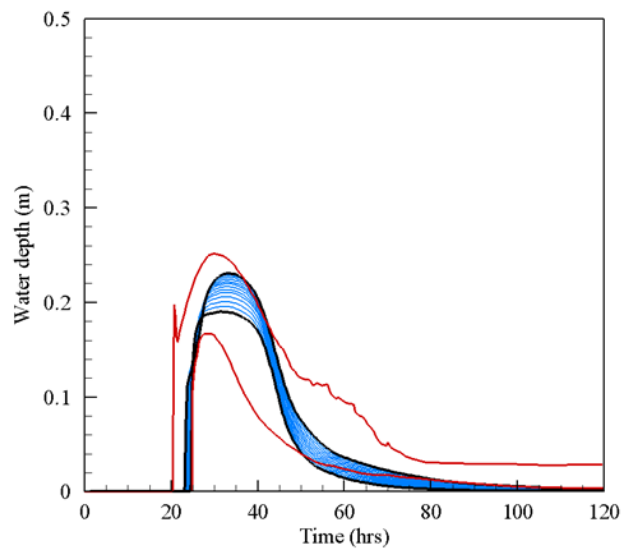


(d)

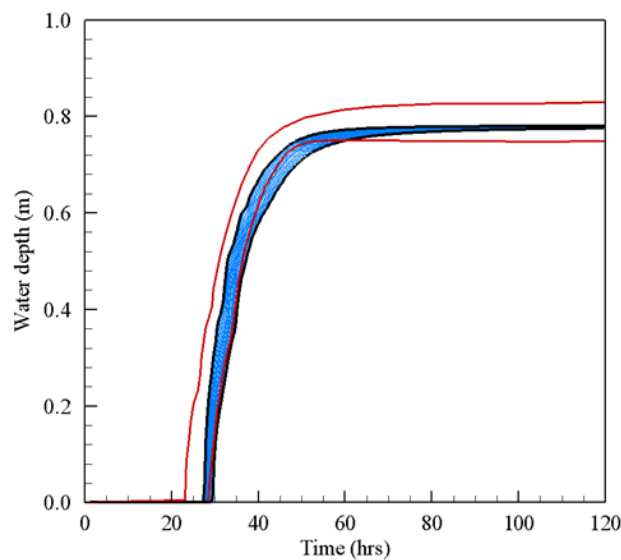
— LISFLOOD-FP (Sim. No. 1) — LISFLOOD-FP (Sim. No. 7)
 — LISFLOOD-FP (Sim. No. 13) — Full 2D model (min & max)



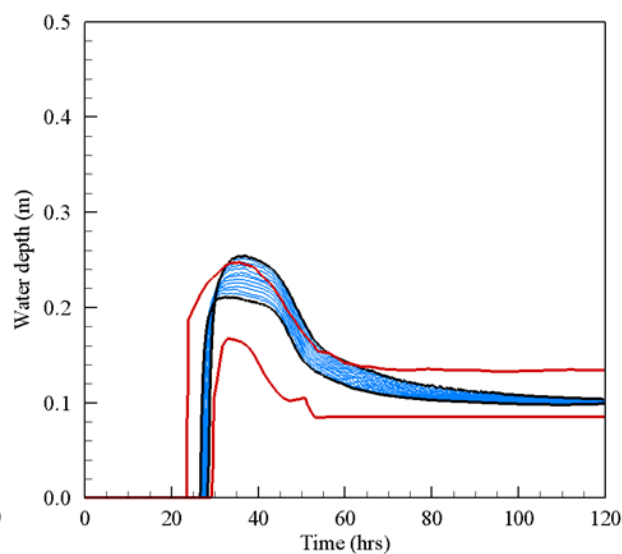
(a)



(b)

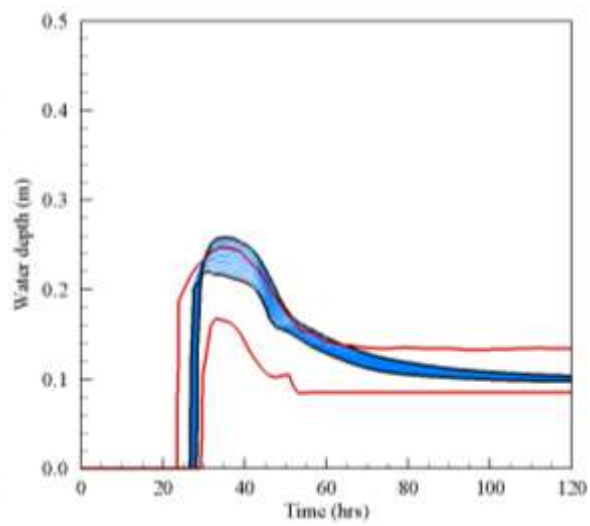
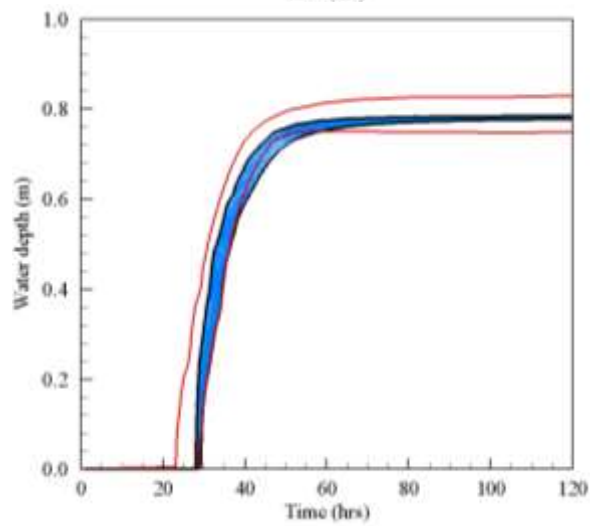
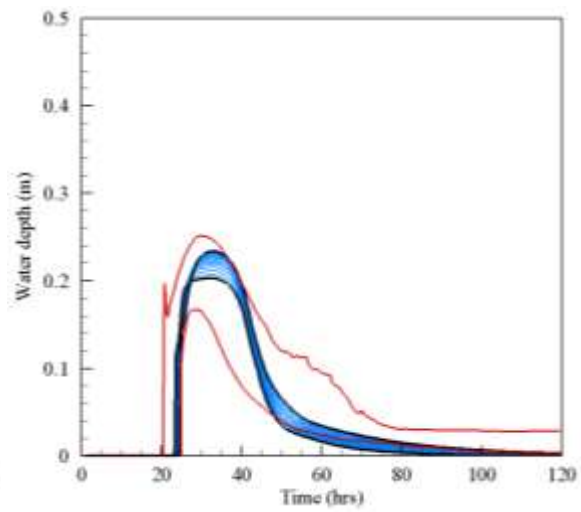
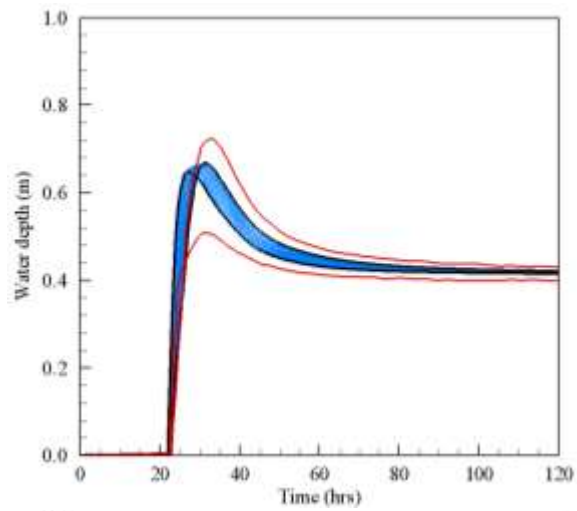


(c)

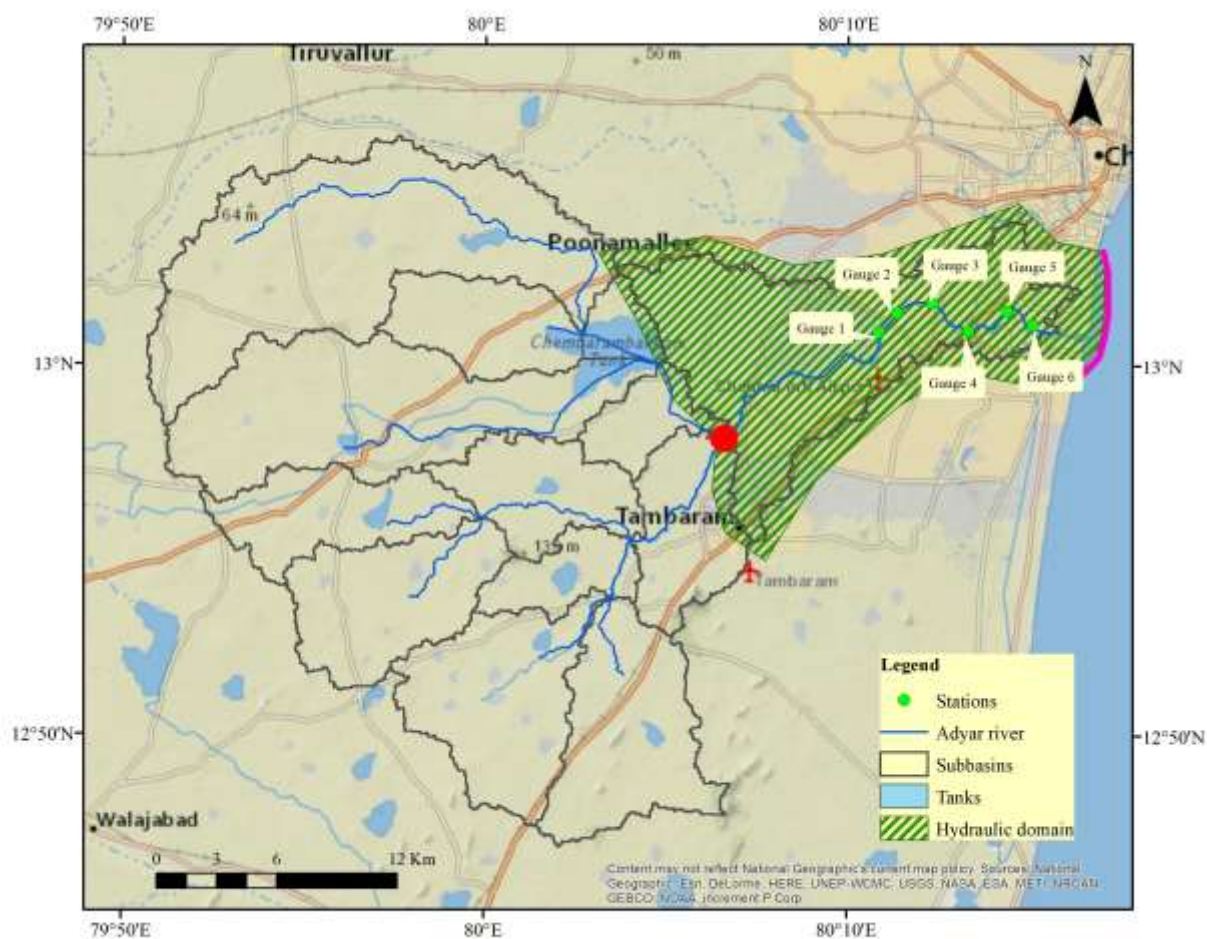


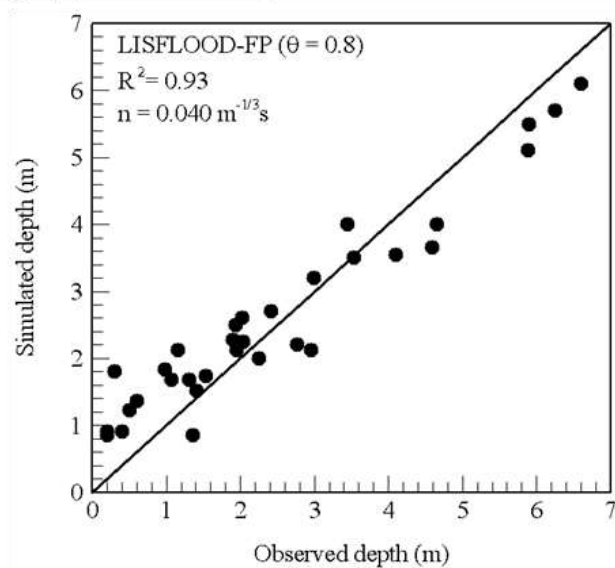
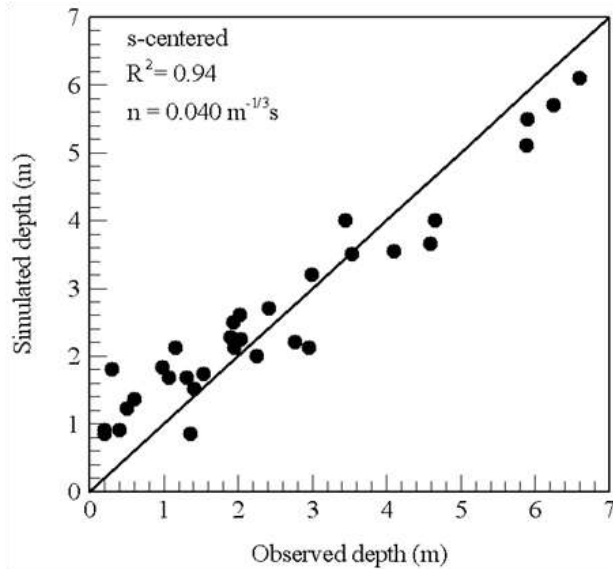
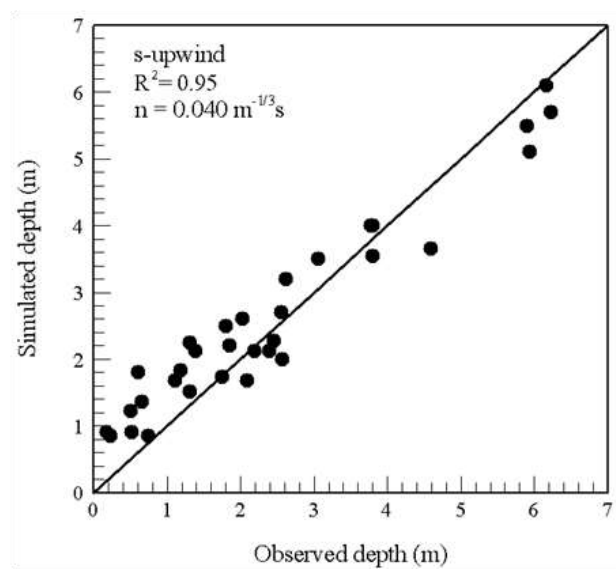
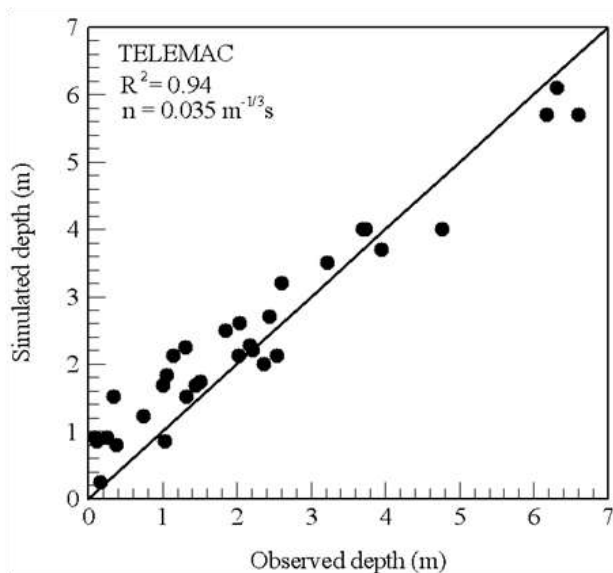
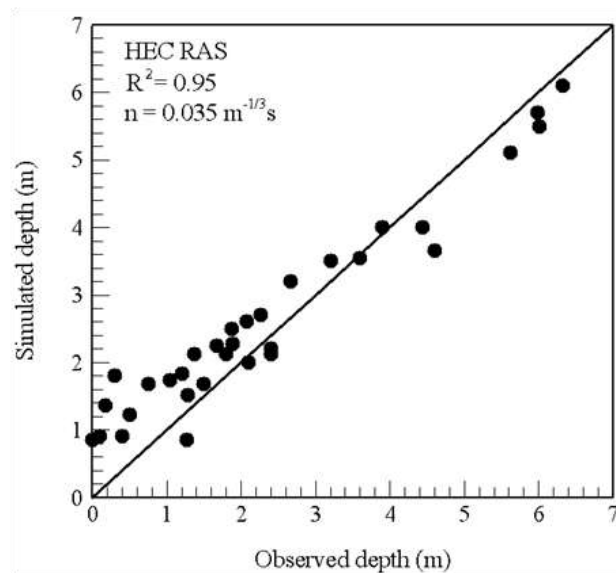
(d)

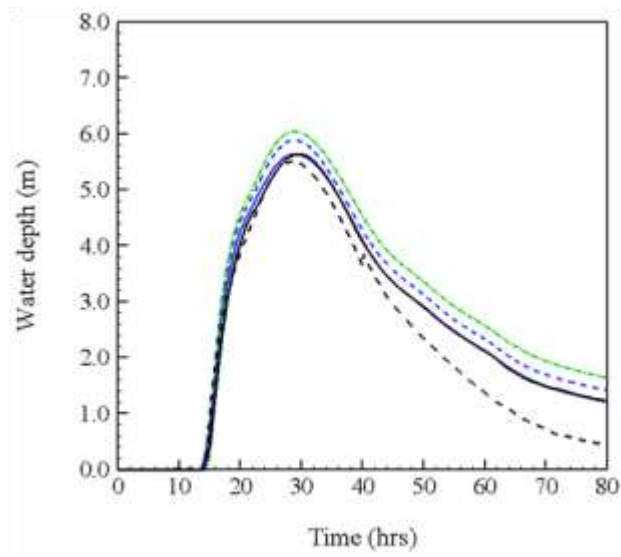
— Ensemble of s-upwind — s-upwind (min & max)
— Full 2D model (min & max)



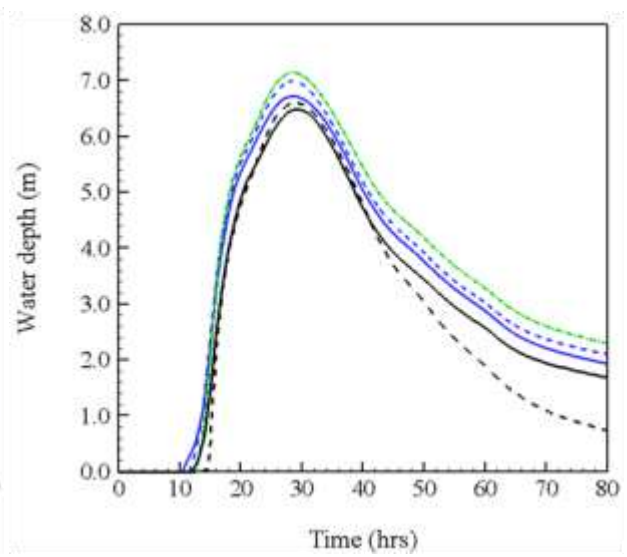
— Ensemble of s-centered — s-centered (min & max) — Full 2D model (min & max)



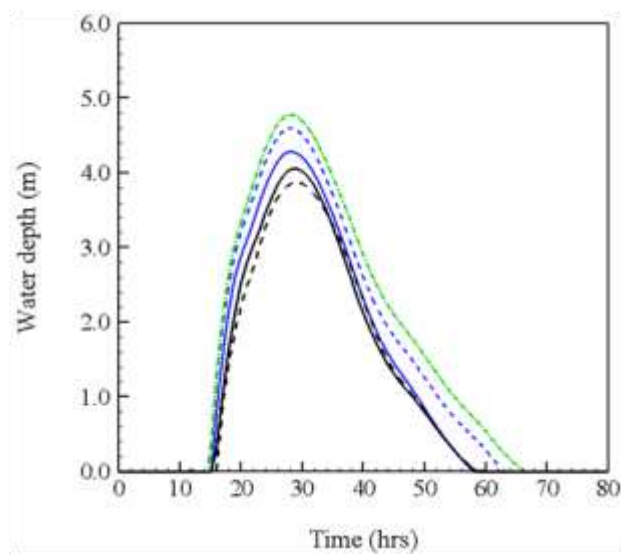




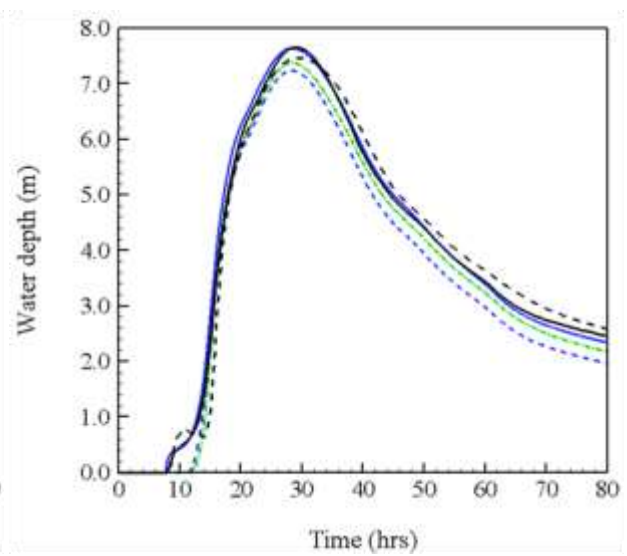
(a)



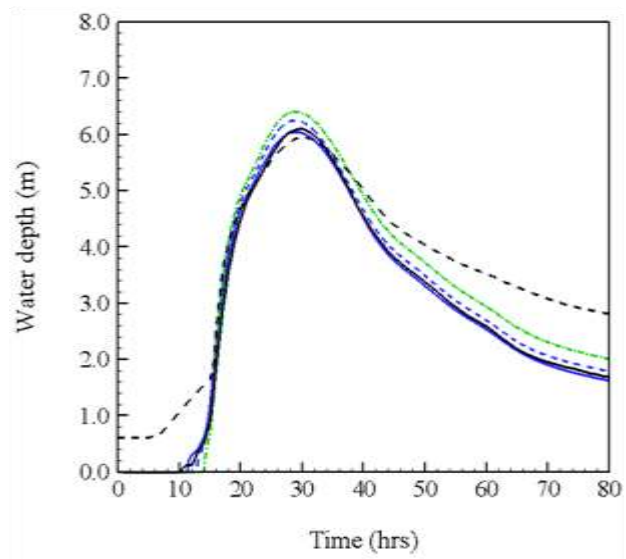
(b)



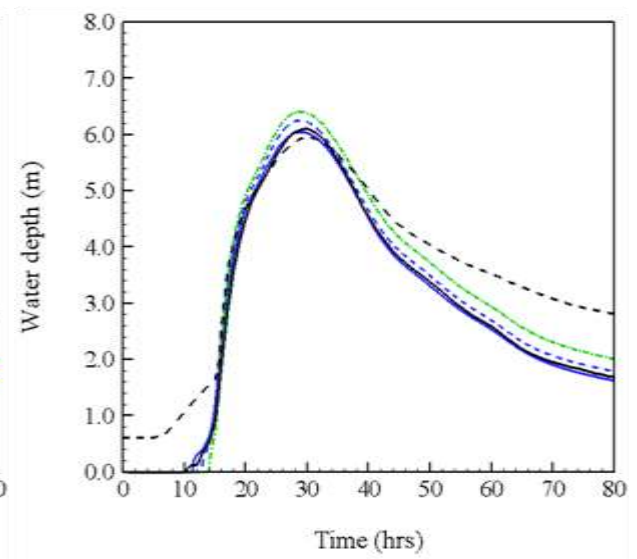
(c)



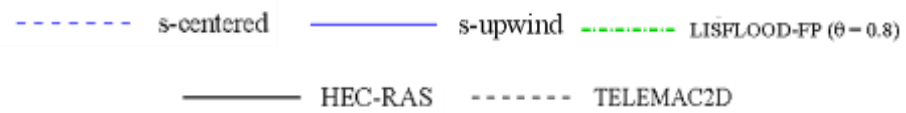
(d)

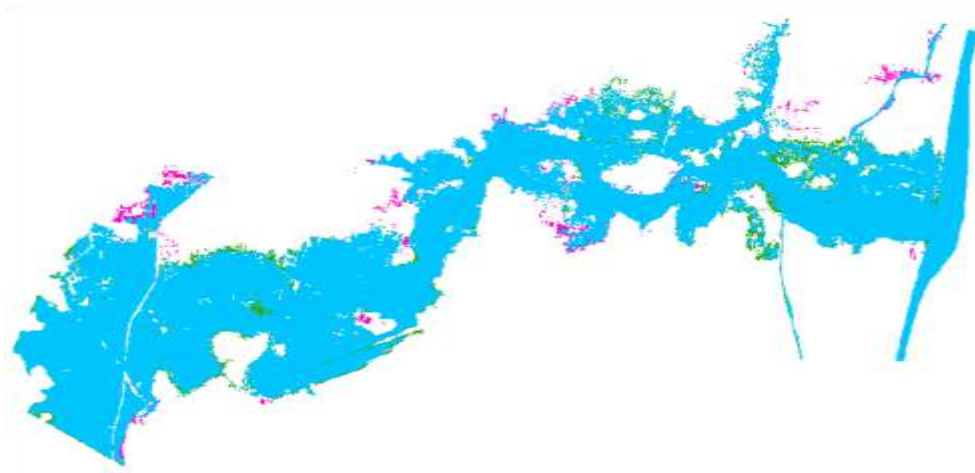


(e)

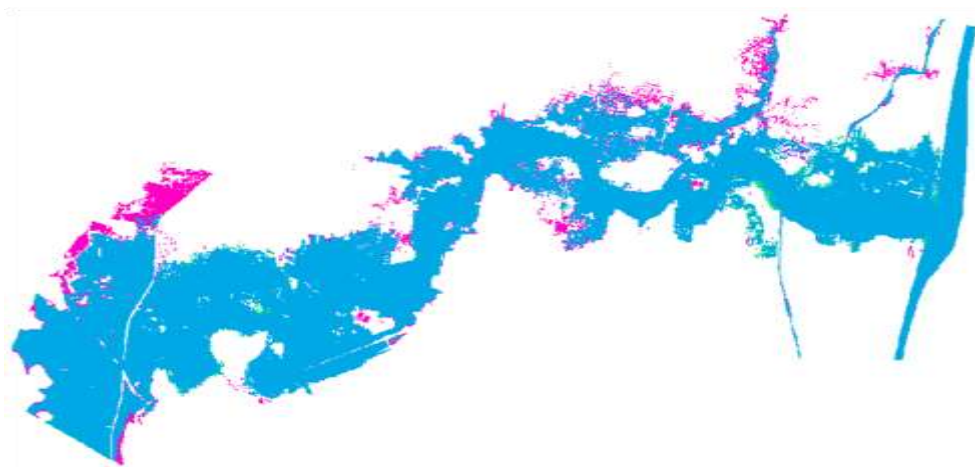


(f)

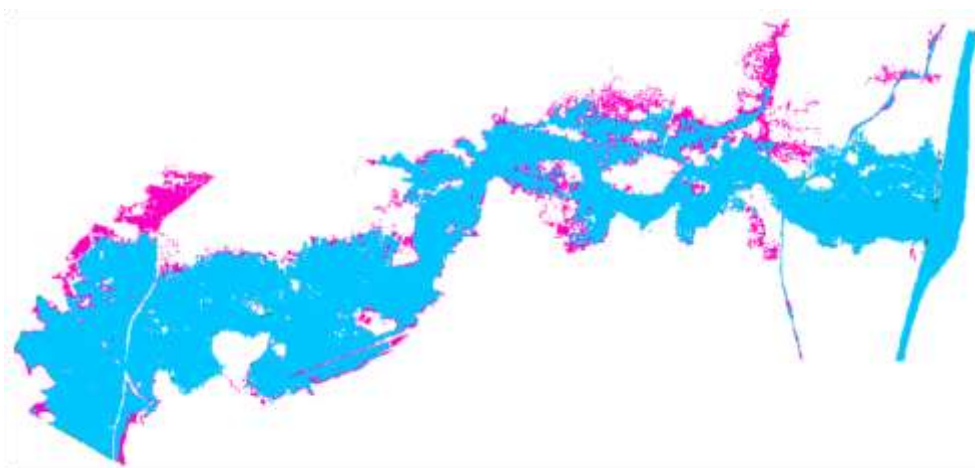




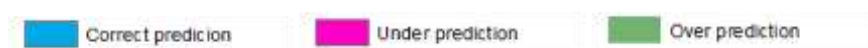
(a)

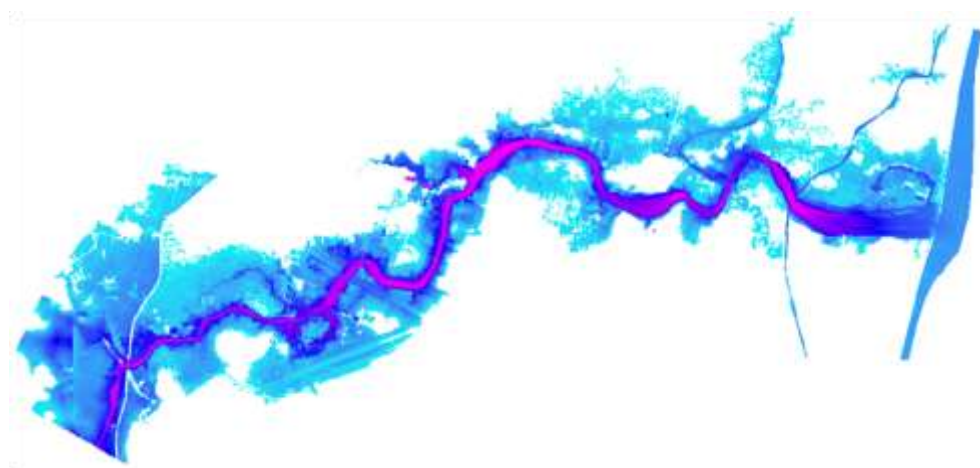


(b)

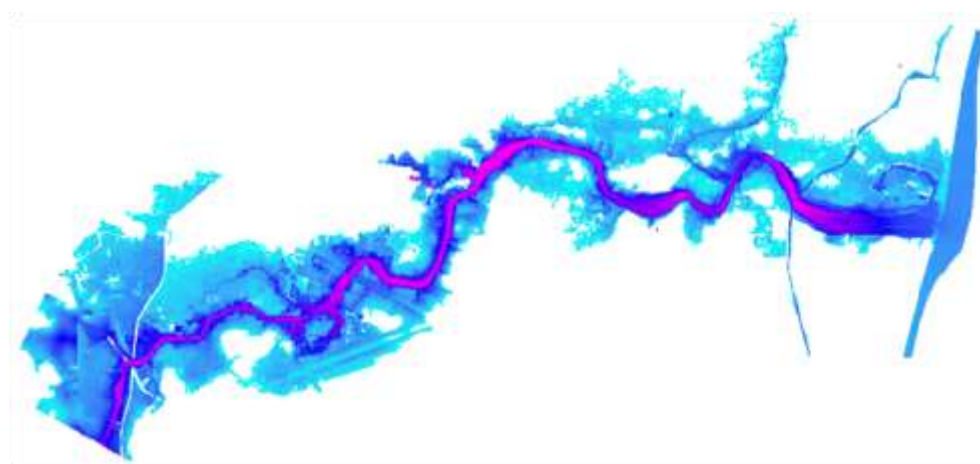


(c)

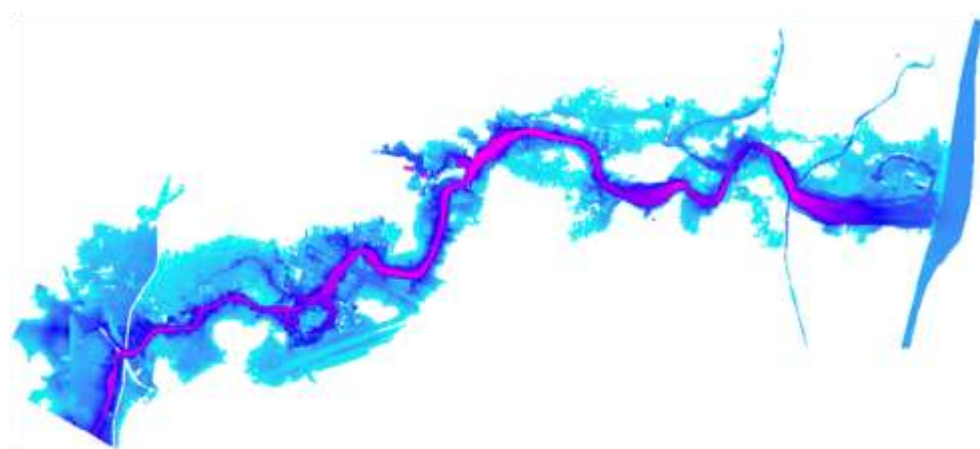




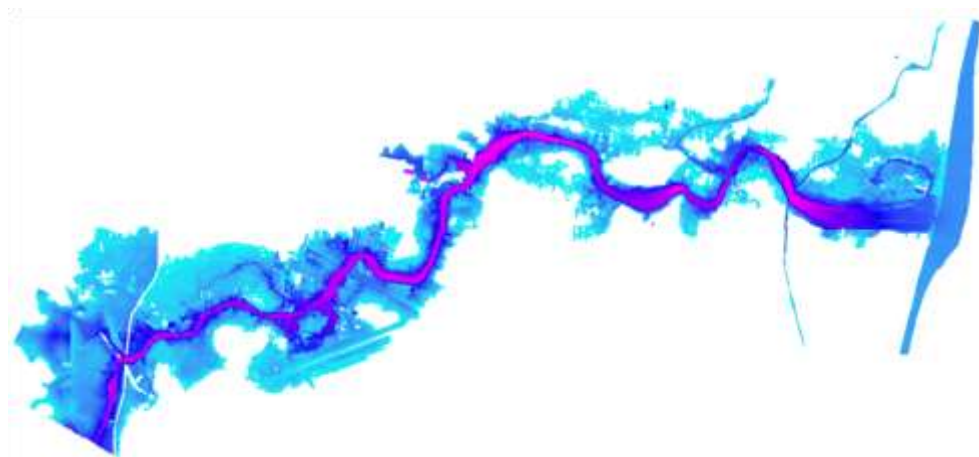
(a)



(b)



(c)



(d)

Water depth (m)

